ELSEVIER

Contents lists available at ScienceDirect

# Chemical Engineering Journal

journal homepage: www.elsevier.com/locate/cej





# The combination of S-doped ZIF-8 with graphene oxide for enhanced near-infrared light photocatalytic and photothermal sterilization

Ziling Zhou<sup>a</sup>, Huiping Zhu<sup>a,b</sup>, Shuilin Wu<sup>c,\*</sup>, Yuelin Lv<sup>a</sup>, Yufeng Zheng<sup>c</sup>, Dafu Chen<sup>d,\*</sup>, Shengli Zhu<sup>e</sup>, Zhaoyang Li<sup>e</sup>, Zhenduo Cui<sup>e</sup>, Xiangmei Liu<sup>a,b,\*</sup>

- <sup>a</sup> Biomedical Materials Engineering Research Center, Collaborative Innovation Center for Advanced Organic Chemical Materials Co-constructed by the Province and Ministry, Hubei Key Laboratory of Polymer Materials, Ministry-of-Education Key Laboratory for the Green Preparation and Application of Functional Materials, School of Materials Science & Engineering, Hubei University, Wuhan 430062, China
- <sup>b</sup> School of Health Science and Biomedical Engineering, Hebei University of Technology, Tianjin 300401, China
- <sup>c</sup> School of Materials Science and Engineering, Peking University, Beijing 100871, China
- d Laboratory of Bone Tissue Engineering, Beijing Laboratory of Biomedical Materials, Beijing Research Institute of Orthopaedics and Traumatology, Beijing JiShuiTan Hospital, Beijing 100035, China
- <sup>e</sup> School of Materials Science & Engineering, The Key Laboratory of Advanced Ceramics and Machining Technology by the Ministry of Education of China, Tianjin University, Tianjin 300072, China

#### ARTICLE INFO

#### Keywords: Photocatalytic Sterilization Wound healing Metal-organic framework Graphene oxide

#### ABSTRACT

The problem of bacterial resistance caused by the overuse of antibiotics was a constant threat to human health. Photocatalytic therapy was an important tool to address this problem but was limited by its photocatalytic properties and biocompatibility. Herein ZIF-8 was doped by sulfur (S) and then combined with graphene oxide (GO) to form a heterojunction (S-ZIF-8/GO). The photocatalytic performance of the composite was significantly enhanced compared to that of the single component. The underlying mechanism is as following factors. On the one hand, S doping induced the formation of the Zn-S bond in ZIF-8, thus improving NIR light absorption and the yields of photogenerated electron-hole pairs. On the other hand, the interface between S-ZIF-8 and GO accelerated the transfer of photogenerated electrons from S-ZIF-8 to GO. In addition, the S-ZIF-8/GO has even better photothermal performance. Further experiments revealed the bacteria-killing mechanism of S-ZIF-8/GO, *i.e.*, the bacterial cell membrane was destroyed with increased permeability by hyperthermia caused by the photothermal effect, allowing the leakage of inside protein and the entrance of ROS into the bacteria to destroy the inside substances. In vivo animal tests showed that the composite was beneficial for wound healing due to the slow release of Zn<sup>2+</sup> ions from S-ZIF-8/GO.

#### 1. Introduction

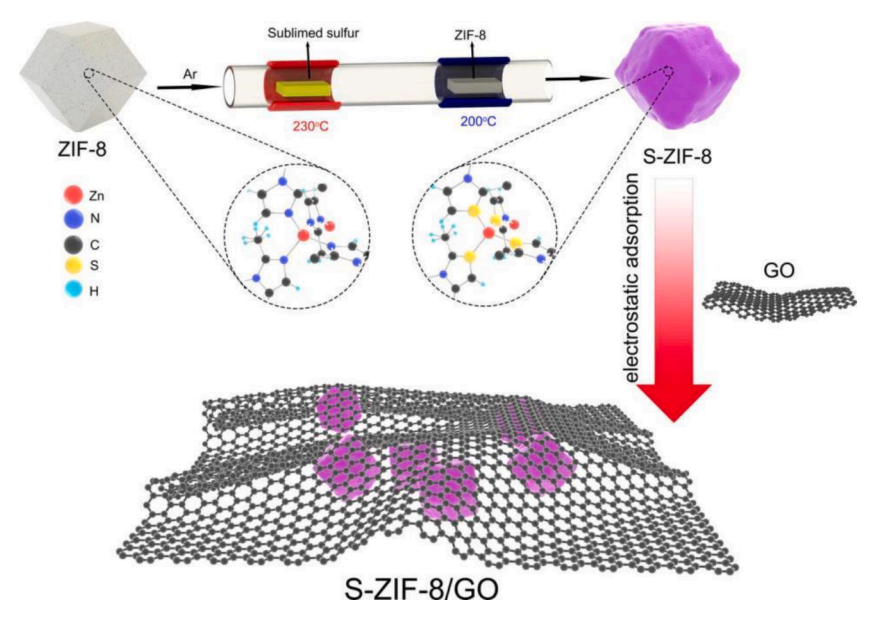
Pathogenic bacterial infection often occurs during the wound healing process, which usually leads to the extension of the healing process and even deterioration of wounds when disinfection is not appropriate and timely [1–3]. Traditional antibiotics treatment for bacterial infections has been proven to cause bacterial resistance and even superbugs due to the abuse/overuse of antibiotics [4–7]. Antibiotic-free strategies have been developed to fight bacterial infections. For example, some endogenous antibacterial materials such as Ag<sup>+</sup>-release materials [8,9], zinc oxide [10,11], Cu<sup>2+</sup>-release materials [12], quaternary ammonium salt

[13,14], and organic antibacterial peptides [15–17], showed effective antibacterial activity. However, the endogenous antibacterial material is a double-edged sword, which can kill bacteria but also bring toxicity to normal cells and tissues. For example, silver ions cannot be excreted from the body and harm the organs after accumulation to a certain concentration [18]. Additionally, the sustainable release of antibacterial factors from these endogenous antibacterial agents leads to bacteria resistance, even for nanosilver [19]. Therefore, it is necessary to develop exogenous antibacterial strategies to treat bacterial infections without inducing toxicity and bacteria resistance.

As one of the important exogenous bacteria-killing strategies,

E-mail addresses: slwu@pku.edu.cn (S. Wu), chendafujst@126.com (D. Chen), liuxiangmei1978@163.com (X. Liu).

<sup>\*</sup> Corresponding authors at: Biomedical Materials Engineering Research Center, Collaborative Innovation Center for Advanced Organic Chemical Materials Coconstructed by the Province and Ministry, Hubei Key Laboratory of Polymer Materials, Ministry-of-Education Key Laboratory for the Green Preparation and Application of Functional Materials, School of Materials Science & Engineering, Hubei University, Wuhan 430062, China.



Scheme 1. S-ZIF-8/GO preparation process.

phototherapy is a portable, low-cost and eco-friendly treatment method for bacterial infections [20–22], which includes photodynamic treatment and photothermal therapy. Some semiconductor materials such as ZnO, TiO<sub>2</sub>, MoS<sub>2</sub>, WS<sub>2</sub>, and g-C<sub>3</sub>N<sub>4</sub> can be excited to produce radical oxygen species (ROS) under light irradiation to kill bacteria [23–27]. However, the photocatalytic performance of these semiconductors is restricted due to the rapid recombination of photogenerated electronhole pairs as well as the lower adsorption ability of oxygen species, resulting in poor ROS yields. It is critical to find suitable photoresponsive materials with enhanced photocatalytic performance and stronger oxygen species adsorption ability.

As one of the metal-organic frameworks (MOF), the microporous structured ZIF-8 is formed by coordinating Zn<sup>2+</sup> with 2-methylimidazole, and this kind of MOF possesses an ultra-high porosity and huge internal surface area [28,29]. The unique structure endows MOF-based materials with various applications such as catalysis [30,31], drug delivery [32], disinfection [33-35]. ZIF-8 has also been utilized for drug delivery for treating cancer and bacterial infections [36,37]. The shortcoming of this material is the poor light absorption ability, rapid recombination of photogenerated electron-hole pairs, and excessive release of Zn<sup>2+</sup>, inducing poor photocatalytic performance and cytotoxicity [38]. Adding heteroatom dopants (B, N, S, and P) to the C matrix is a feasible strategy for creating defects and impressively improving adsorption capacity and catalytic performance [39]. Among the alien atoms, S was recognized as a preeminent dopant for creating defects [40]. Recent studies have shown that introducing S into composites can lead to increased interfacial electron transfer, NIR light absorption ability, and a decrease in the recombination rate of electron-hole pairs [41,42]. According to previous reports, modulating the electronic structure of MOFs with S under thermodynamic conditions can produce greater intrinsic activity and optimal adsorption energies, leading to exceptional photocatalytic performance and improved chemical stability [43]. Furthermore, it has been reported that some two-dimensional materials such as  $Ti_3C_2T_x$ , GO and  $MoS_2$  nanosheet have excellent photocatalytic or photothermal properties, and can be used to tune the bandgap of semiconductors by forming heterojunction with them, thus improving the photocatalytic performance of the materials [44–46].

In view of the above-mentioned, we propose a hypothesis whether a composite can be constructed by combining S-doped ZIF-8 with GO, which has stronger NIR light absorption ability and enhanced photocatalytic performance than a single component, thus possessing powerful photocatalytic bacteria-killing ability. Based on the

hypothesis, as shown in Scheme 1, in a double temperature zone tube furnace, the synthesized ZIF-8 MOF was doped by sublimed S, then combined with GO by electrostatic adsorption. During doping process, the S replaced the N in ZIF-8 partially to form Zn-S bonds with Zn nodes. Theoretic calculation disclosed that the Zn-S bond in S-ZIF-8/GO attracted photogenerated electrons and accelerated their transfer from S-ZIF-8 to GO.

#### 2. Experimental method

## 2.1. Preparation of ZIF-8

We prepared ZIF-8 by growing metal  $\rm Zn^{2+}$  and organic imidazolate linkers in methanol (CH<sub>3</sub>OH) using coordination chemistry solutions according to previously reported methods [47]. Using a typical synthesis process, we solubilized 2.75 g of 2-methylimidazole and 2.293 g of Zn (NO<sub>3</sub>)<sub>2</sub>·6H<sub>2</sub>O in 100 mL of CH<sub>3</sub>OH, respectively, and whisked for 2 h. We washed the obtained ZIF-8 3 times using CH<sub>3</sub>OH and left it to dry in an oven for 24 h at 40 °C.

## 2.2. Preparation of S-ZIF-8

We positioned 0.88 g S powder upstream in the tube furnace, and 0.08 g ZIF-8 downstream. Next, we filled the tube furnace with Ar gas. We maintained the temperature zone on the sublimation-S side at 230  $^{\circ}\text{C}$  and the temperature zone on the ZIF-8 side at 200  $^{\circ}\text{C}$  for 2 h under flowing Ar. Thereafter, when the tube furnace cooled, we collected S-ZIF-8.

## 2.3. Preparation of S-ZIF-8/GO and ZIF-8/GO

We mixed 20 mL of deionized water (DI) with 0.04 g of GO to obtain solution A, then treated solution A with ultrasonic dispersion for 2 h, mixed it with 0.16 g of S-ZIF-8, and whisked it for 24 h. We obtained S-ZIF-8/GO after centrifugation of the products, then washed it three times in ethanol and DI, and dried it. We prepared ZIF-8/GO to study the photocatalytic mechanism of S-ZIF-8/GO. We prepared ZIF-8/GO in the same way as S-ZIF-8/GO, except that we used ZIF-8 instead of S-ZIF-8.

## 2.4. Photothermal performance testing of materials

We prepared 0.1 mg/mL aqueous solution samples separately and

placed 500  $\mu L$  of aqueous solution in 1.5 mL EP tubes. We irradiated the EP tubes with 808 nm NIR light (0.24 W/cm²) for 20 min, using DI as a control (Ctrl), and recorded temperature changes with a thermal camera. We obtained the heating–cooling curve of S-ZIF-8/GO (0.1 mg/mL) under 808 nm NIR light irradiation and calculated its photothermal conversion efficiency ( $\eta$ ) according to the following equation [48]:

$$\eta = [hS \times (T_{\text{max}} - T_0) - Q] / [I \times (1 - 10^{-A})]$$

In the formula, h, S,  $T_{\text{max}}$ ,  $T_0$ , Q, I, and A denote the heating transfer coefficient, surface area of the heated area, maximum temperature, ambient temperature, heat absorption energy of the orifice plate, power of the 808 nm laser, and absorbance of samples at 808 nm, respectively.

During the cooling process, we calculated the time constant ( $\tau_s$ ) according to the following equation:

$$t = -\tau_s \times \ln\theta = \ln(T - T_0)/(T_{\text{max}} - T_0)$$

Then, assuming that the temperature of the system was highly stable, with the heat input equal to the heat output, we used the following equation:

$$hS = m_s \times C_s/\tau_s$$

In the formula,  $m_s$  and  $C_s$  are the mass and specific heat capacities of water, respectively.

#### 2.5. Material characterization

We employed field emission scanning electron microscopy (FE-SEM, OPTON, SIGMA500, China) and high-resolution transmission electron microscopy (HRTEM, FEI, FEI Tecnai 12, USA) to investigate the morphology of the synthesized samples. We used energy-dispersive spectroscopy (EDS) to analyze the elemental distributions of the synthesized materials, and employed X-ray diffraction (XRD, D8A25, Bruker, Germany) to analyze the crystalline phases of the samples. We studied the elemental constitution of the materials using X-ray photoelectron spectroscopy (XPS, ESCALAB 250Xi, Thermo Scientific, USA). We investigated the diffuse reflectance spectra of the synthesized samples using an ultraviolet-visible (UV-vis) spectrophotometer (UV-3600, Shimadu, JP). We assessed the photothermal and photocatalytic properties of the synthesized samples under an 808 nm light (LOS-BLD-0808, China), recorded the temperature changes in the synthesized samples using a thermal imager (FLIR-E50, FLIR-SYSTEMS-Inc, USA), and analyzed the photoluminescence (PL) spectra with a fluorescence spectrometer (LS-55, PE, USA).

#### 2.6. Photoelectrochemical testing

We investigated the photoelectrochemical properties of the materials using an electrochemical workstation (CHI660E, China) and performed photocurrent and electrochemical impedance spectroscopy (EIS) tests using an 808 nm NIR light source (0.24  $W/cm^2)$  with a 71.021 g/L  $Na_2SO_4$  solution as the electrolyte. To prepare the working electrode, we thoroughly mixed 3 mg of sample and 200  $\mu L$  of Nafion with 1 mL of DI, and then we dripped 150  $\mu L/mL$  of the mixed solution onto the ITO glass electrode and dried it.

## 2.7. ROS test

We detected ROS generation in the samples with 2',7'-dichlorofluorescein (DCFH) under 808 nm (0.24 W/cm²) NIR light irradiation and reacted the DCFH with ROS to generate fluorescence that was detectable with a microplate reader. We added  $160~\mu L$  of prepared DCFH solution to a 96-well plate, and then transferred  $40~\mu L$  of aqueous sample solution (0.5 mg/mL) to the wells. We measured the ROS yields of the samples every 2 min using the microplate reader after 20 min of irradiation with an 808 nm NIR light. The trapping reagent to detect

superoxide anion  $(\cdot O_2^-)$  was 5,5-dimethyl-1-pyrrolin-*N*-oxide (DMPO), and 200  $\mu L$  aqueous solution of the material (0.5 mg/mL) and 1  $\mu L$  trapping reagent under 808 nm NIR light irradiation. We used 2,2,6,6-tetramethylpiperidine (TEMP), 200  $\mu L$  of aqueous solution of the material (0.5 mg/mL), and 1  $\mu L$  of trapping reagent as the trapping reagent to detect singlet oxygen ( $^1O_2$ ) under 808 nm NIR light irradiation. We employed electron spin resonance (ESR, JES-FA200, JEOL, Japan) to detect  $\cdot O_2^-$  and  $^1O_2$  in the sample generation.

#### 2.8. Theoretical calculations

We used the Vienna *ab initio* simulation package (VASP) to calculate the spin-polarized density functional theory (DFT) of the samples based on the Perdew–Burke–Ernzerhof (PBE) formulation within the generalized gradient approximation (GGA). The ionic cores were described as adopting projected augmented wave (PAW) potentials using a planewave basis set with a kinetic energy cutoff of 450 eV to account for valence electrons. When the energy change was smaller than  $10^{-5}$  eV, we considered the electronic energy self-consistent, but when it was lower than 0.02 eV  $\rm \mathring{A}^{-1}$ , we considered the geometry optimization convergent. The vacuum spacing was 18  $\rm \mathring{A}$  in a direction perpendicular to the plane of the structure. We employed the DFT + D3 method to depict weak interactions based on Grimme-scheme empirical corrections.

#### 2.9. Antibacterial tests

We used the plate-coating method to evaluate the antibacterial actions of the materials against *Staphylococcus aureus* (*S. aureus*) in the synthesized samples *in vitro*. We placed 160  $\mu$ L of *S. aureus* (10<sup>7</sup> CFU/mL) and 40  $\mu$ L of aqueous sample solution (0.5 mg/mL) in 96-well plates. While one group of samples was not irradiated with light, the other group was treated with 808 nm NIR light (0.24 W/cm²) irradiation for 20 min. Thereafter, we evenly coated 20  $\mu$ L of mixed solution onto agar plates, cultivated it at 37 °C in an oven for 24 h, and recorded and calculated the antibacterial rate. We calculated the antibacterial efficiency of the experimental group using the following equation: antibacterial rate (%) = [1-(CFU\_experimental group/CFU\_control group)]  $\times$  100 %.

Bacterial SEM: Following completion of the antibacterial process, we placed the bacterial solution in a refrigerator for 2 h, discarded the supernatant in the well plate, retained the precipitate, and added glutaraldehyde to fix the bacteria. After completing the bacterial fixation, we washed the bacterial precipitate with phosphate-buffered saline (PBS) three times. We then dehydrated the bacteria using a gradient with different ethanol concentrations for 15 min at a time. Thereafter, when the precipitate dried, we adopted SEM to observe and photograph the bacterial morphology.

Protein leakage: We detected bacterial protein leakage using a bicinchoninic acid disodium (BCA) reagent. First, we mixed 40  $\mu L$  of aqueous sample solution (0.5 mg/mL) with 160  $\mu L$  of  $10^7$  CFU/ $\mu L$  bacteria liquid containing S. aureus and irradiated the mixture with 808 nm light for 10 min. We centrifuged the bacterial solution at 4 °C and 6000 rpm/min after 20 min of 808 nm light irradiation. We added the supernatant of each group to 200  $\mu L$  of BCA reagent and placed the mixed solution in an incubator at 37 °C for 30 min. Thereafter, we measured the optical density (OD) value of 562 nm of the mixed solution using a microplate reader.

Bacterial cell membrane permeability assay: After completing the light-induced antibacterial process, we handled the mixed solution with an ortho-nitrophenyl-beta-galactoside (ONPG) kit. This used a microplate reader, and the OD value of the supernatant was analyzed at 420 nm.

Cellular reactive oxygen species detection: We used a ROS assay kit to measure intracellular ROS. Before adding the samples, we incubated  $10^7$  CFU/mL of bacteria in 96-well plates with a DCFH-DA diluent (10  $\mu$ L), followed by irradiation for 20 min. We left the bacterial solution for

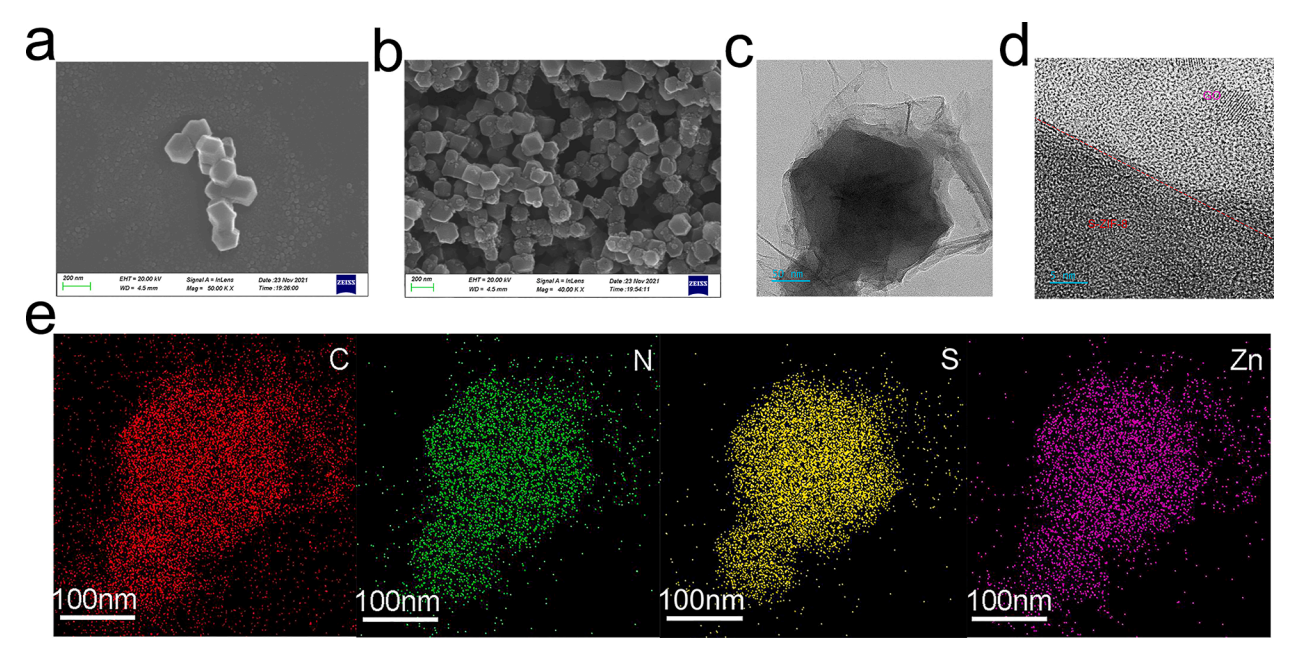


**Fig. 1.** a) SEM morphology of ZIF-8 (scale bar = 200 nm). b) SEM morphology of S-ZIF-8 (scale bar = 200 nm). c) TEM morphology of S-ZIF-8/GO (scale bar = 50 nm). d) HRTEM image of S-ZIF-8/GO (scale bar = 5 nm). e) Elemental distribution of S-ZIF-8/GO (scale bar = 100 nm).

4 h before removing the supernatant from the wells, retained the precipitate, dried it, and photographed it using fluorescence microscopy.

## 2.10. Cytocompatibility evaluation

Cell toxicity assay: We used NIH-3T3 cells and 3-[4,5-dimethylthiazol-2-yl]-2,5-diphenyl-etrazoliumbromide (MTT) to investigate the cytotoxicity of the synthetic samples using a cell toxicity assay. We sterilized the samples with UV irradiation and immersed them in cell medium (0.1 mg/mL) for 24 h after centrifugation to extract a solution, which we then used in subsequent cell experiments. After incubating the NIH-3T3 cells for 24 h in 96-well plates, we discarded the cell medium and added 200  $\mu L$  of solution extracted from different samples to the wells. We incubated the solution with NIH3T3 cells for 24 h. Thereafter, we removed the cell medium before injecting 200  $\mu L$  PBS solution of MTT (0.5 mg/mL) into the 96 wells and culturing it for a further 4 h at 37 °C. After removing the MTT solution, we added 200  $\mu L$  of dimethyl sulfoxide (DMSO) and shook the mixture for 15 min. Finally, we subjected the supernatant liquid to OD value measurement with a microplate reader (490 nm).

Cell Morphology: After coculturing NIH3T3 cells for 12 h, we rinsed the cells in 96-well plates three times with sterile PBS and fixed them in 4 % formaldehyde for 10 min. We stained the cells with FITC for 30 min, and thereafter rinsed the cells 3 times with PBS, stained them for 30 s with DAPI, and washed them 3 times with PBS. We obtained cell morphology images with an inverted fluorescence microscope.

Hemolytic Rate Test: We performed hemolysis tests with fresh mouse (Balb/c) blood. We centrifuged the blood at 3000 rpm/min for 15 min and discarded the supernatant to collect red blood cells. We then washed the red blood cells three times with saline and dispersed them in saline. We mixed 0.5 mL of saline solution with the samples (0.2 mg/mL) with 0.5 mL of 10 % red blood cell dispersion. After incubating the mixed solution at 37 °C for 4 h, we centrifuged it at 3000 rpm for 15 min. We then determined the OD value of the supernatant at 570 nm using a microplate reader. The negative control was saline, and the positive control was water. We calculated the hemolytic rates (RHR %) of the samples using the following equation: RHR (%) = (A<sub>Sample</sub>-A<sub>PBS</sub>)/(A<sub>water</sub>-A<sub>PBS</sub>).

#### 2.11. In vivo animal assay

For this experiment, we obtained male BALB/c mice (weight 18-20 g each) from Huazhong Agricultural University Animal Hospital. The Animal Research Committee of Tongji Medical College, Huazhong University of Science and Technology, Wuhan, authorized the experimental animal protocol. We conducted all experimental procedures according to the Animal Administration Regulations of the Ministry of Health of the People's Republic of China and the Guidelines for the Care and Use of Laboratory Animals in China. We separated the mice into three groups (Ctrl, 3 M, and S-ZIF-8/GO), which we further divided into 3 time groups of 2, 5, and 10 days, with 12 mice in each group. After anesthesia, we made wounds in the backs of the mice with tools, and we mixed a 20 µL bacteria solution (10<sup>8</sup> CFU/mL) with 1 mg/mL of S-ZIF-8/ GO (experimental group). After 808 nm light irradiation for 20 min, we applied standard wound dressings to the 3 M group, fed the mice in a suitable environment, and then examined and photographed the wounds at 2, 5, and 10 days. Each time, we sacrificed three mice from each group to perform routine blood tests. We also excised the wounds and surrounding skin and stained the wounds with Giemsa and hematoxylin and eosin (H&E) for 2 days, 5 days, and 10 days, respectively. We used two stains to assess the bacterial infection of the wounds. To assess the biological toxicity of S-ZIF-8/GO, we removed the kidneys, spleens, livers, hearts, and lungs of the mice at 10 days and stained them with H&E.

### 3. Results and discussion

### 3.1. Characterization of the material

The SEM images revealed that ZIF-8 had a dodecahedron structure (Fig. 1a). The morphology of ZIF-8 was not altered after S doping, and the morphology of S-ZIF-8 resembled that of ZIF-8. The corresponding SEM images are depicted in Fig. 1b. The elemental mapping, illustrated in Fig. S1a and b, showed that the C, N, Zn, and S elements were well distributed across the S-ZIF-8 sample. The TEM images of S-ZIF-8/GO revealed that S-ZIF-8 had a dodecahedron structure and GO had a wrinkled thin-layer structure (Fig. 1c). The TEM images and energy-dispersive spectroscopy maps disclosed sufficient contact between GO and S-ZIF-8 (Fig. 1d) and homogeneous distributions of S, N, C, and Zn in

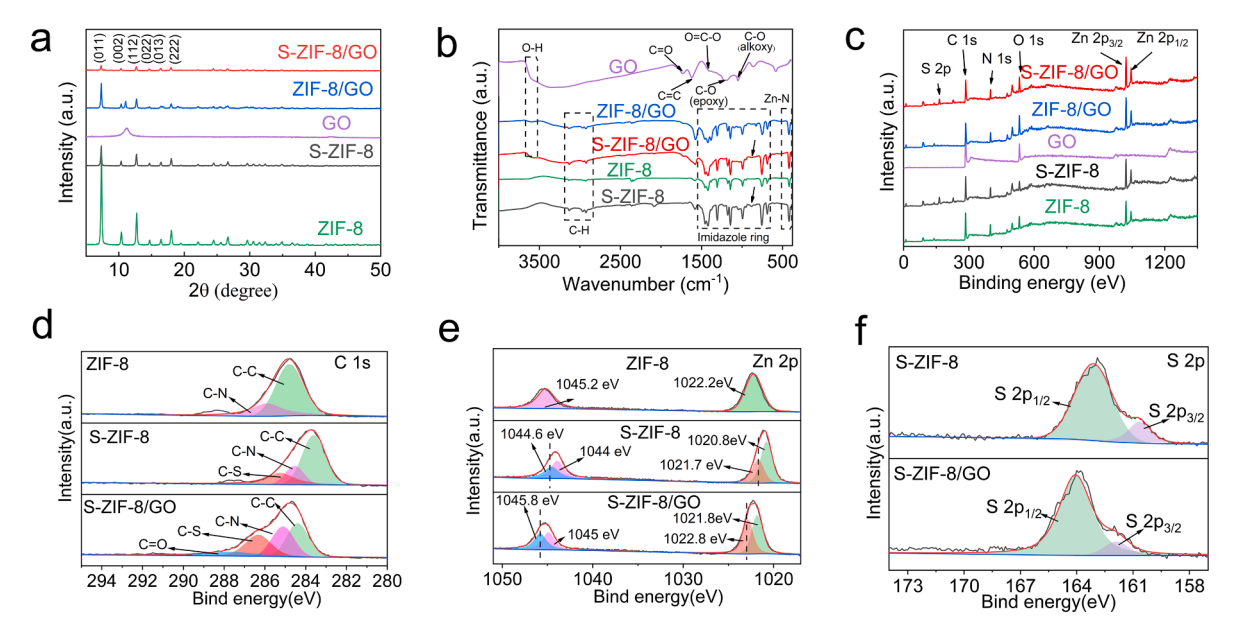


Fig. 2. a) XRD patterns. b) FT-IR patterns. c) XPS spectra. d) C 1 s high-resolution scanned images of ZIF-8, S-ZIF-8, and S-ZIF-8/GO. e) Zn 2p high-resolution scanned images of ZIF-8, S-ZIF-8, and S-ZIF-8/GO. f) S 2p high-resolution scanned images of S-ZIF-8 and S-ZIF-8/GO.

the S-ZIF-8/GO (Fig. 1e). The boundary between S-ZIF-8 and GO in Fig. 1d indicated excellent integration, and the HRTEM image confirmed that GO was successfully combined with S-ZIF-8. From the dynamic light scattering (DLS) data, we observed that the S-ZIF-8/GO dispersed homogeneously in water, with an average size of about 100–1000 nm (Fig. S2).

Through XRD, we identified the phase structure (Fig. 2a). The ZIF-8 showed characteristic peaks at 7.3°, 10.3°, 12.8° and 18.25°, which corresponded to crystal planes (011), (002), (112), and (222), respectively, as previously reported [49]. No significant new characteristic peaks were found in the XRD spectra of S-ZIF-8, indicating that the introduction of S into the ZIF-8 particles did not alter their crystal phase structure. This phenomenon suggests that S incorporation might be achieved by replacing some of the atoms in the ZIF-8 framework [50]. After GO incorporation, the XRD images of S-ZIF-8/GO resembled those of ZIF-8/GO. The peaks at 11° of ZIF-8/GO corresponded to the characteristic diffraction peak of GO [51]. As shown in Fig. 2a, the intensity of the characteristic diffraction peak of the GO signal declined due to the low GO content in ZIF-8/GO [52]. Regarding S-ZIF-8/GO, the characteristic diffraction peak of GO at  $11^{\circ}$  was absent, which can be attributed to the distortion of the stacked GO [53]. However, the predominant diffraction patterns of S-ZIF-8 remained in S-ZIF-8/GO, although the intensity of the peaks decreased. These patterns were consistent with the composition of the S-ZIF-8/GO, since S-ZIF-8 was the main component.

To investigate further, we studied the functional groups in S-ZIF-8 and S-ZIF-8/GO using Fourier transform infrared spectroscopy (Fig. 2b). ZIF-8 showed a characteristic peak of the imidazole ring from 650 cm<sup>-1</sup> to 1550 cm<sup>-1</sup> and a Zn–N chemical bond peak at 424 cm<sup>-1</sup>. We attributed the characteristic peaks at 3135 cm<sup>-1</sup> and 2937 cm<sup>-1</sup> in ZIF-8 to the unsaturated hydrocarbons C-H and C-H(CH<sub>3</sub>), respectively [54]. After S doping, the previous functional groups in S-ZIF-8 still existed. Moreover, the peak at 800–900 cm<sup>-1</sup> formed a new S-based bond in the S-ZIF-8 [43]. S-ZIF-8/GO and ZIF-8/GO exhibited a typical GO peak at 3,606 cm<sup>-1</sup> after the addition of GO, which corresponded with the O-H bond [55–59]. In conclusion, the presence of characteristic S-ZIF-8 peaks with GO in S-ZIF-8/GO demonstrated that GO was successfully doped with S-ZIF-8.

The XPS survey spectra (Fig. 2c) for ZIF-8 consisted of diffraction peaks for Zn, C, and N elements, and S-ZIF-8 comprised Zn, C, N, and S element diffraction peaks. The S diffraction peak revealed that S was successfully doped with ZIF-8. After adding GO, the O peak was present

in the XPS survey spectra of ZIF-8/GO and S-ZIF-8/GO and belonged to GO. Fig. 2d shows the C 1 s XPS spectrum. The high-resolution C 1 s spectrum in ZIF-8 showed that it belonged to the C-N and C-C bonds at 285.9 eV and 284.8 eV, respectively. After S doping, we observed C-N and C-C bond peaks at 284.6 eV and 283.6 eV, respectively. The C-C and C-N bond peaks of S-ZIF-8 shifted to a lower energy than that of pure ZIF-8, suggesting that S introduced negative charges [43]. The zeta potential implied that S doping introduced a negative charge, ZIF-8 was positively charged, and the potential of S-ZIF-8 decreased significantly after S doping (Fig. S3). The emergence of a characteristic peak at about 285.3 eV also demonstrated a combination of C and S, suggesting that S probably replaced the N atom, formatting the C-S bonds [60,61]. Fig. S4 presents the N 1 s XPS spectrum. The high-resolution spectrum of N 1 s in ZIF-8 showed that it belonged to the Zn-N and C-N bonds at 399.4 eV and 398.8 eV, respectively. After S doping, the characteristic peaks at 399.1 eV and 398.6 eV shifted to a lower energy than in pure ZIF-8. As shown in Fig. 2e, compared with ZIF-8 and S-ZIF-8, the Zn 2p peaks of S-ZIF-8 shifted to a lower energy. The binding energies at 1044.6 and 1021.7 eV in S-ZIF-8, and 1045.8 eV and 1022.8 eV in S-ZIF-8/GO, could be attributed to the formation of a Zn-based band with S in S-ZIF-8, confirming the successful intramolecular modulation related to Zn bonding [43,62]. The high-resolution spectrum of S 2p at 160.65 eV and 163.12 eV in S-ZIF-8 (Fig. 2f). The peak deconvoluting into two peaks centered at 160.65 eV and 163.12 eV belonged to S, confirming chemically bonded S moieties in S-ZIF-8. These phenomena indicate that the S elements were successfully doped in the S-ZIF-8 sample by replacing lattice N to form new bonds (Zn-S) [55,63].

We conducted a BET test on the materials (Fig. S5). The BET surface area of ZIF-8 was 555.997  $\rm m^2g^{-1}$ . After S doping, the BET surface area of S-ZIF-8 increased to 634.592  $\rm m^2g^{-1}$  (Fig. S5a), which could have resulted from embedded S altering the pore structure of ZIF-8. Small quantities of weakly bonded imidazole molecules were removed from ZIF-8 at 200 °C, at which time the S combined with ZIF-8, enlarging the pore size of ZIF-8 [64]. After reaching room temperature, some of the S particles entered the pore structure and formed larger pore sizes [65]. After adding GO, the BET surface area of ZIF-8/GO was 40.741  $\rm m^2g^{-1}$ , and the BET surface area of S-ZIF-8/GO was 492.803  $\rm m^2g^{-1}$ . A significant reduction in the BET surface area of ZIF-8/GO may be attributable to the collapse of part of the structure of ZIF-8/GO (Fig. S1c), whereas S-ZIF-8/GO could still maintain the complete structural morphology (Fig. S1d). The H<sub>2</sub>O molecules changed the hydrophobic–hydrophilic

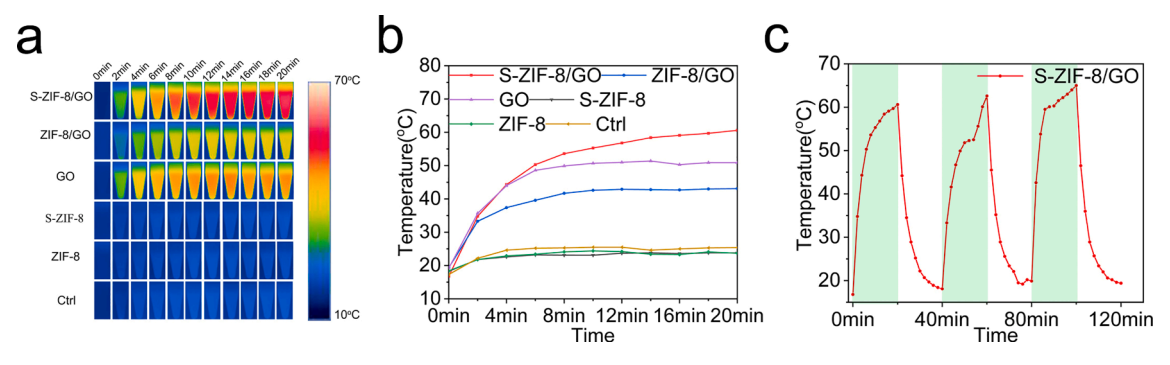


Fig. 3. Photothermal and photocatalytic properties of the samples tested. a) Real-time infrared thermal images. b) The photothermal heating curves of samples. c) Photothermal cycle curves of S-ZIF-8/GO.

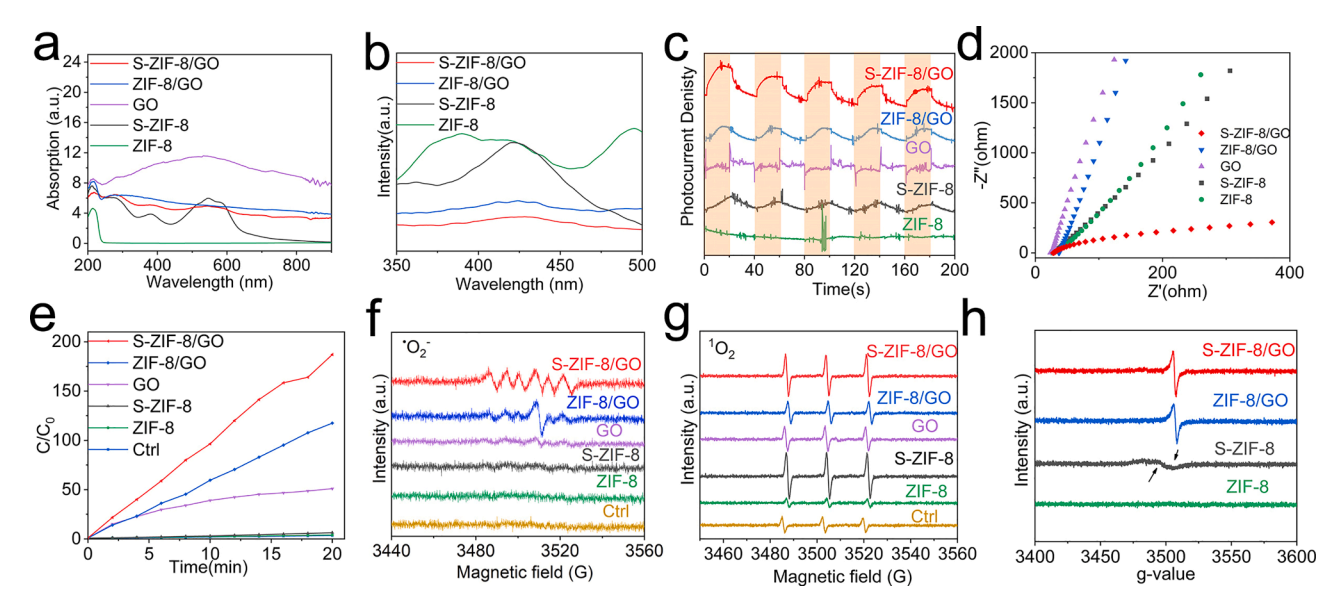


Fig. 4. Photocatalytic properties of the samples tested. a) UV spectra. b) PL spectra. c) Photocurrent denisty of the samples. d) EIS of samples. e) ROS production of samples detected by DCFH when irradiated with 808 nm NIR light. f)  $\cdot O_2^-$  spectra of samples. g)  ${}^1O_2$  spectra of samples. h) EPR spectra.

balance of ZIF-8, causing  $OH^-$  ions to attack the unsaturated Zn or N sites and subsequently inducing the destruction of Zn–N bonds in ZIF-8 frameworks [47]. After S doping, S partially replaced the N atom, which made the S-doped ZIF-8 structure more stable, and the Zn–S bond could not be destroyed by  $H_2O$ . By comparing the pore sizes of these materials (Fig. S5b), we found that the doping of S and GO hardly changed their pore size distribution.

#### 3.2. Photothermal and photocatalytic performance

Fig. 3a and b display the photothermal properties of the materials. Under 808 nm NIR light irradiation, GO had excellent photothermal properties, and the temperature of GO reached 50 °C, but pure S-ZIF-8 and ZIF-8 exhibited no obvious photothermal properties. After combining ZIF-8 with GO, the ZIF-8/GO nanocomposite increased the temperature to 40 °C. After S-ZIF-8 was added to GO, the S-ZIF-8/GO had the highest temperature, at approximately 60.6 °C. Fig. S6 illustrates the linear regression curve of the negative natural logarithm of temperature and time of S-ZIF-8/GO and ZIF-8/GO during the cooling phase. The  $\eta$  value was calculated based on the results of the time constant for heat transfer and the maximum steady-state temperature. The S-ZIF-8/GO sample had a higher  $\eta$  value (29.264 %) than the ZIF-8/GO sample (27.567 %). According to reports, the photothermal conversion efficiency of S-ZIF-8/GO was much higher than that of conventional photothermal nanomaterials, such as Au nanorods (21 %) and

Cu<sub>9</sub>S<sub>5</sub> (25.7 %) [66,67]. S-ZIF-8/GO could generate a large amount of heat under 808 nm NIR light irradiation, since it contained many more electron loops between the S-ZIF-8 and GO for electron motion [68,69]. The temperature of S-ZIF-8/GO exhibited a stable on/off effect under 808 nm NIR light irradiation (Fig. 3c), indicating that S-ZIF-8/GO exhibited excellent photothermal stability.

We evaluated the optical characteristics of the materials using UV-vis diffuse reflectance spectra. The absorption value shows the lighttrapping ability; the larger the value, the stronger the ability to absorb light. The absorption characteristic peaks of ZIF-8 were distributed in the UV region, with poor absorption in the NIR region (Fig. 4a). After combining S-doped ZIF-8 with GO, the S-ZIF-8/GO exhibited a greater NIR light-absorption capacity. The S doping of ZIF-8 reduced the band gap, making it easier for photogenerated electrons to be excited and transferred to GO. A greater charge transfer induced greater electron ring production, which resulted in excellent photothermal properties [68,70]. The PL spectra revealed the recombination rates of the photogenerated electrons in the samples. The PL spectrum in Fig. 4b exhibited the highest fluorescence intensity for ZIF-8 compared to the other samples. The PL spectrum showed a lower fluorescence intensity for S-ZIF-8/GO than for the other samples. This phenomenon suggests that S doping combined with GO could decrease the recombination rate of ZIF-8 electron-hole pairs.

Fig. 4c shows the photocurrent densities of the synthesized samples under 808 nm light irradiation. The photocurrent density of S-ZIF-8/GO

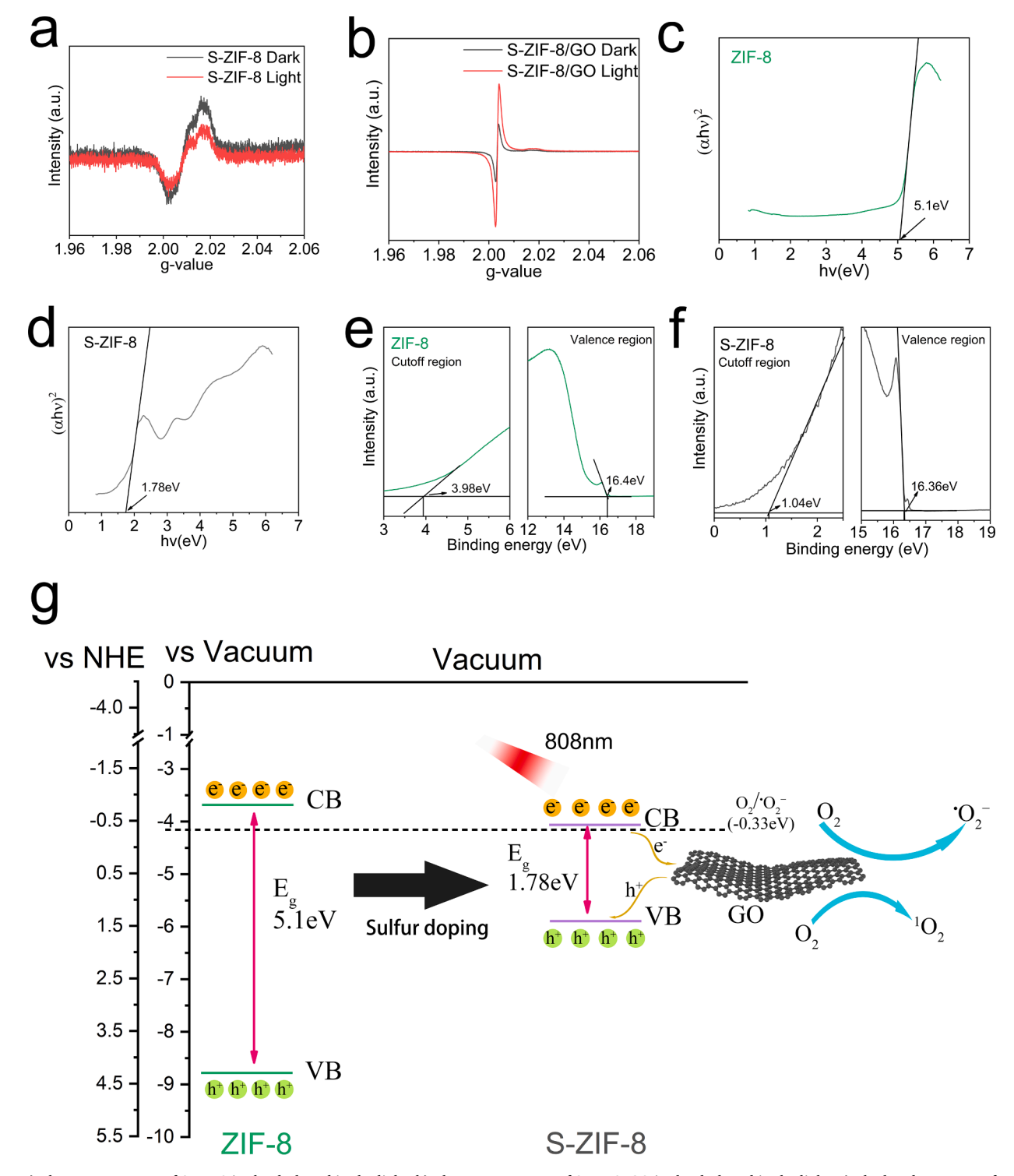


Fig. 5. a) The EPR spectrum of S-ZIF-8 in the dark and in the light. b) The EPR spectrum of S-ZIF-8/GO in the dark and in the light. c) The band structure of ZIF-8 as calculated by its UV–visible absorption spectrum. e) UPS spectra of ZIF-8. f) UPS spectra of S-ZIF-8. g) The photocatalyst mechanism schematic diagram of S-ZIF-8/GO under 808 nm light irradiation.

was stronger than that of the other samples, demonstrating the excellent photogenerated electron transfer capability of S-ZIF-8/GO under 808 nm light irradiation. We used EIS to analyze the impedance of the synthesized materials. Fig. 4d shows that S-ZIF-8/GO exhibited the smallest slope of the curves, indicating the smallest impedance of S-ZIF-8/GO. The EIS and photocurrent density measurements indicated that the interface formation between S-ZIF-8 and GO decreased impedance and facilitated the rapid transfer of photogenerated electrons.

We used DCFH to measure the total ROS yield. After 20 min of 808 nm light irradiation, S-ZIF-8/GO exhibited the highest yield of ROS (Fig. 4e). We detected the ESR signal using capture reagents DMPO and TEMP to study the type of ROS generated in the samples. DMPO dye detected  $\cdot O_2^-$  and TEMP dye detected  $^1O_2$ . Following 808 nm light irradiation, S-ZIF-8/GO exhibited the highest yield of  $\cdot O_2^-$  and  $^1O_2$  (Fig. 4f and g). Fig. S7 shows the ROS yield of S-ZIF-8/GO under 808 nm light irradiation after three cycles. It was evident that as the cyclic

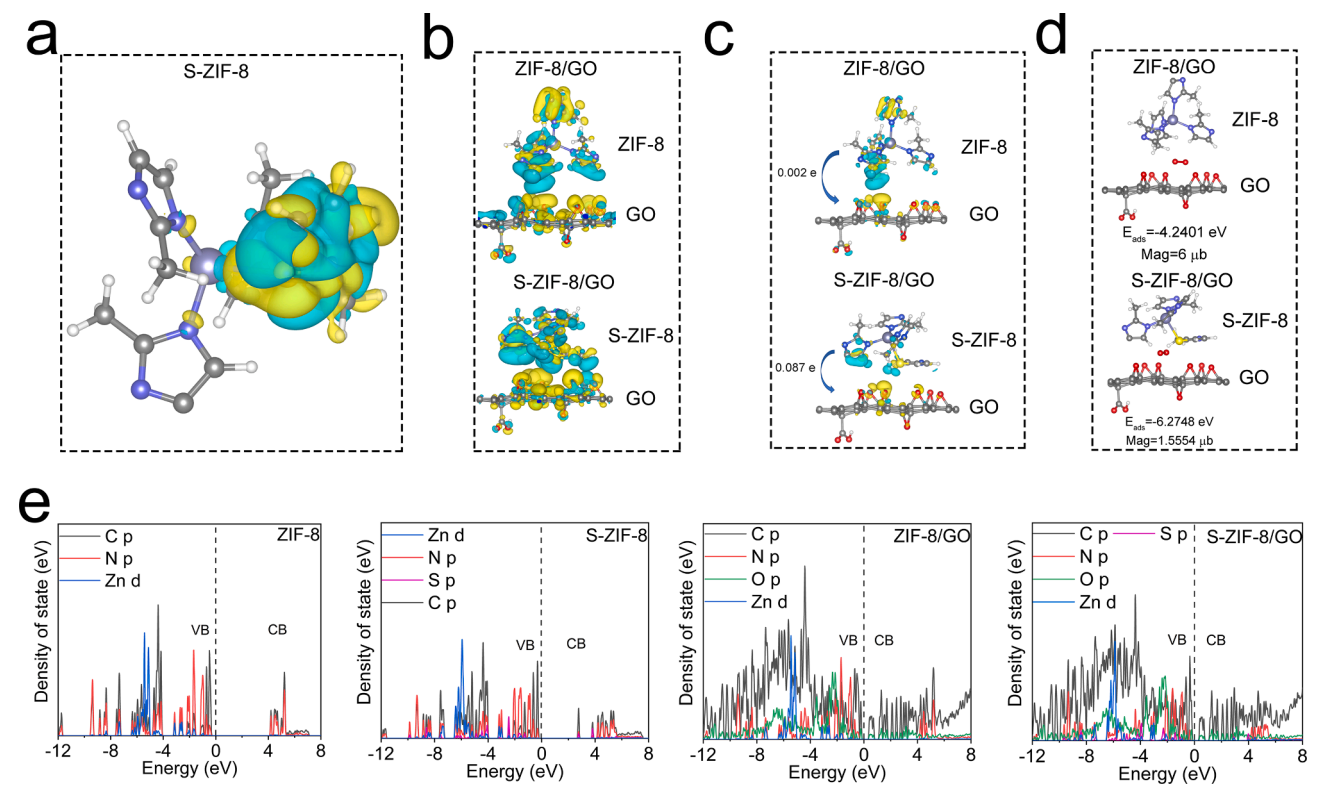


Fig. 6. Theoretical calculations. a) Charge density difference of S-ZIF-8. b) Charge density difference of ZIF-8/GO and S-ZIF-8/GO. c) Bader charge of ZIF-8/GO and S-ZIF-8/GO. d) O<sub>2</sub> adsorption energies, magnetic moment (Mag). e) Density of electronic states.

number of irradiations increased, the ROS yield of S-ZIF-8/GO decreased, implying that the composite had poor catalytic stability after recycling three times. The XRD patterns of the S-ZIF-8/GO composite before and after three consecutive 808 nm light irradiations are shown in Fig. S8. Fig. S8 reveals that after three consecutive 808 nm light irradiations, S-ZIF-8/GO exactly matched the diffraction peak of the without-light irradiations S-ZIF-8/GO, indicating that S-ZIF-8/GO had excellent stability.

Fig. 4h shows the EPR spectra for each material, illustrating the strong symmetric signals caused by these electron excess centers. This could be inferred from the increase in signal intensity, indicating that the local electron excess concentration in S-ZIF-8 increased compared to ZIF-8, suggesting that the electron density of ZIF-8 changed, and electron excess centers increased, after S doping [71]. The strongest signal was observed when we combined S-ZIF-8 with GO, caused by the unsaturated bonds in GO and the electron excess centers introduced by S doping. The results showed that ZIF-8 was doped by S and then combined with GO to form a heterojunction that enhanced photocatalytic efficiency [72].

## 3.3. Photocatalytic mechanism

We characterized the EPR spectra of S-ZIF-8 and S-ZIF-8/GO with and without light irradiation. The EPR spectra recorded in Fig. 5a show the ESR signals of S-ZIF-8, for which the intensity decreased after light irradiation. The Zn–S bond could be used as a charge trapping site [54]. After S doping ZIF-8, Zn–S bonds trap electrons to form holes in ZIF-8. After light irradiation, electrons are excited to "neutralize" these holes, resulting in a decrease in signal intensity [73]. The EPR spectrum recorded in Fig. 5b shows the signal of S-ZIF-8/GO, which became stronger after light irradiation, indicating that the photogenerated electrons were transferred from S-ZIF-8 to GO under 808 nm light irradiation.

According to the Kubelka-Munk formula, we calculated the band

structure of S-ZIF-8/GO (Fig. 5c and d) from the UV-vis spectra in Fig. 4a [74]. We further analyzed the energy band structure of the sample using ultraviolet photoelectron spectroscopy (UPS) detection. From the UPS spectra of the materials (Fig. 5e and f), we computed the work function ( $\Phi$ ) of ZIF-8 and S-ZIF-8 as 4.82 eV and 4.86 eV, respectively. We computed the Fermi energy levels (E<sub>F</sub>) of ZIF-8 and S-ZIF-8 as -4.82 eV and -4.86 eV, respectively. The low binding energy tail ( $E_{\text{edge}}$ ) was the source of the energy gap between the valence band  $(E_{\text{VB}})$  and  $E_{\text{F}}.$  Therefore, the  $E_{\text{VB}}$  and the conduction band  $(E_{\text{CB}})$  of ZIF-8 were 4.3 eV and -0.8 eV, respectively. The  $E_{VB}$  and  $E_{CB}$  of S-ZIF-8 were 1.4 eV and -0.38 eV, respectively. Based on the preceding analysis, the electronic energy band structures of ZIF-8 and S-ZIF-8 are shown in Fig. 5g. The S doping caused the energy gap of S-ZIF-8 to narrow, resulting in stronger photocatalytic properties. Under 808 nm light irradiation, S-ZIF-8 produced photogenerated electron-hole pairs and GO as an electron acceptor of S-ZIF-8, transferring the electrons in S-ZIF-8 to GO, which restricted the recombination of electron-hole pairs, thus improving the photocatalytic properties of S-ZIF-8/GO and generating a high amount of  $\cdot O_2^-$  and  ${}^1O_2$ .

### 3.4. Theoretical calculations

We studied the photocatalytic mechanism of S-ZIF-8/GO further using DFT theoretical calculations. As for S-ZIF-8, the charge density difference (CDD) plot showed the charge distribution between the Zn–S bond (Fig. 6a), electron accumulation (yellow region), and depletion (blue region). The CDD of S-ZIF-8 showed electron accumulation at the Zn–S bond, creating a substantial charge distribution and indicating that the Zn–S bond could promote the separation of the electron–hole pair and provide a faster electron transfer channel. The CDD plot showed the charge distribution between S-ZIF-8 and GO, which suggested that a built-in electric field was formed at the interface, facilitating electron transfer (Fig. 6b). To quantitatively investigate the changes in charge and transfer, we performed a Bader charge analysis of the composite

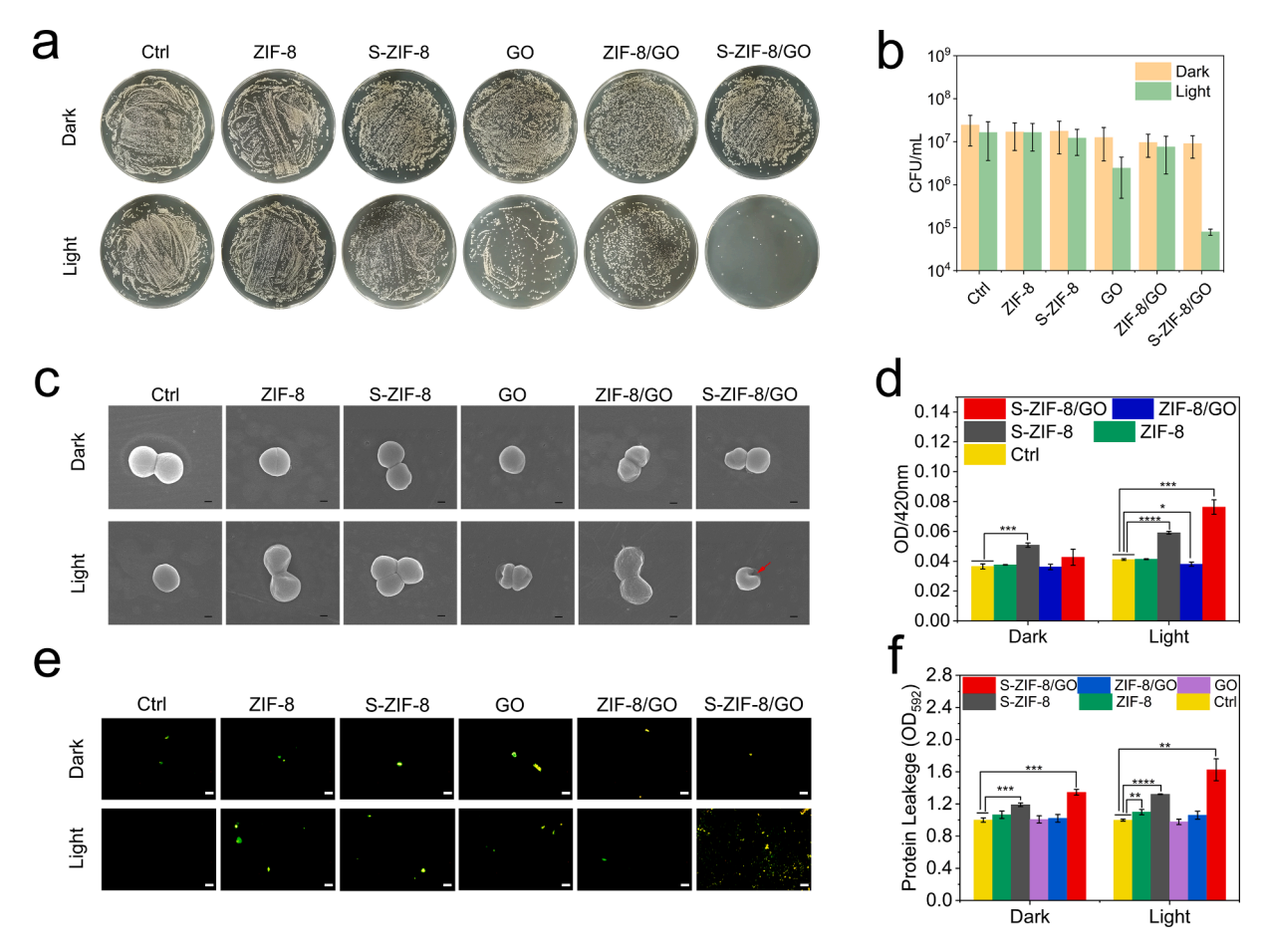


Fig. 7. a) Results of *S. aureus* plate coating after samples were treated with dark or 808 nm near infrared light. b) Antibacterial rate with dark or 808 nm light. c) Bacterial morphology under different treatment conditions characterized by SEM (scale bar = 200 nm). d) Bacterial membrane permeability assay of each group of materials under 808 nm light irradiation and no light irradiation conditions. e) Fluorescence staining images of *S. aureus* treated by samples with DCFH-DA probe (scale bar = 50  $\mu$ m). f) Detection of bacterial protein leakage under 808 nm NIR light irradiation and dark conditions for each group of materials (n = 3, means  $\pm$  SD). \*p < 0.05, \*\*p < 0.01, \*\*\*p < 0.01.

material. Fig. 6c shows a 0.002 electron charge from ZIF-8 to GO, which increased to a 0.087 electron charge due to the existence of the Zn-S bond. The results showed that the Zn-S bond accelerated the transfer of electrons from S-ZIF-8 to GO, which was beneficial for enhancing the photocatalytic performance of the heterojunction [75,76]. It has been reported that the transfer of foreign electrons to O2 is a feasible way to change its spin state and achieve oxygen activation [77]. Since O2 played a significant role in the photocatalytic generation of ROS, we computed the adsorption energy and magnetic distance (Mag) of O2 at the S-ZIF-8/GO and ZIF-8/GO interfaces according to the DFT calculations (Fig. 6d). The oxygen adsorption energy of ZIF-8/GO (-4.24 eV) was higher than that of S-ZIF-8/GO (-6.27 eV), demonstrating that the S-ZIF-8/GO had a strong oxygen absorption capacity. O2 had a spin-flip limitation, which the activation of O<sub>2</sub> needed to overcome [78]. It is known that a lower Mag of O2 means a higher degree of spin-flip. We found that the Mag of S-ZIF-8/GO (1.5554 µb) was lower than that of ZIF-8/GO (6  $\mu$ b), implying greater activation of O<sub>2</sub> in S-ZIF-8/GO.

The density of the electronic states (DOS) of ZIF-8 (Fig. 6e) showed that the valence band (VB) of ZIF-8 was primarily sourced from the 2p state of N and C atoms and the 3d state of Zn atoms, and the CB was primarily sourced from the 2p state of N and C atoms, suggesting that the organic ligands primarily contributed to the VB and CB of ZIF-8, whereas the Zn ions primarily contributed to the VB. The introduction of S altered the VB of ZIF-8, demonstrating the likelihood that the S atom interacted principally with the organic ligand of ZIF-8. Adding the S energy level could decrease the energy of the electron leap necessary to promote electron separation and transfer. After combining ZIF-8 with GO, the VB

of the ZIF-8/GO was primarily sourced from the 2p state of O, N, and C atoms and the 3d state of Zn atoms. We observed greater Fermi energy-level hybridization, indicating that GO promoted electron transfer in ZIF-8. After combining S-doped ZIF-8 with GO, more Fermi energy-level hybridization became evident in S-ZIF-8/GO, demonstrating that the simultaneous addition of S and GO enhanced the electron transfer in ZIF-8. From the theoretical calculations and tests of photocatalytic performance, we inferred that the Zn–S bond in S-ZIF-8/GO could facilitate the separation of electrons and holes, accelerating the transfer of electrons from S-ZIF-8 to GO, and thus allowing the photogenerated electrons to bind  $O_2$  and activate  $O_2$  to produce ROS.

#### 3.5. In vitro antibacterial activity

We determined the antibacterial effect of the synthesized samples against *S. aureus* using the plate-coating method. These samples exhibited almost equal bacterial colonies after 20 min of incubation without light irradiation (Fig. 7a and b), and the results revealed that the samples exhibited no significant antibacterial activity against *S. aureus* under dark conditions. In contrast, few bacterial colonies appeared in the S-ZIF-8/GO group after 20 min of 808 nm NIR light irradiation, indicating that S-ZIF-8/GO exhibited the strongest antibacterial action against *S. aureus*. In Fig. 7b, the S-ZIF-8/GO had an antibacterial rate of 99.6 %. This excellent antibacterial rate may be attributed to the fact that the Zn–S bond promoted the transfer of electrons from S-ZIF-8 to GO, preventing the recombination of electron–hole pairs and enabling S-ZIF-8/GO to generate a high enough temperature and a large amount of

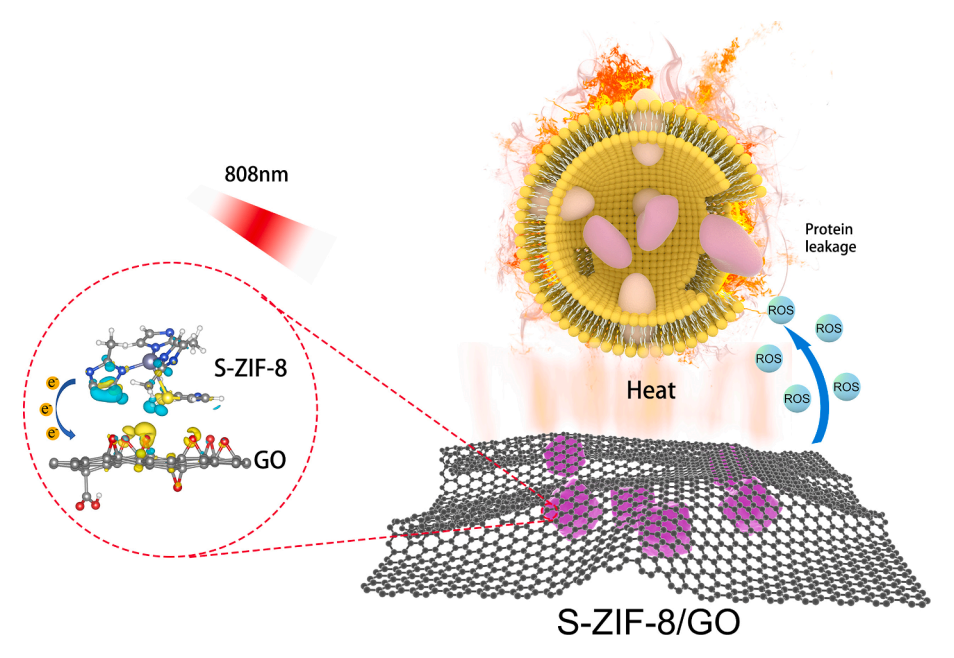


Fig. 8. S-ZIF-8/GO antibacterial mechanism diagram.

ROS to sterilize.

FE-SEM further revealed bacterial morphologies that proved the antibacterial effects of the synthesized samples (Fig. 7c). All groups of bacteria were smooth and intact without 808 nm light irradiation, confirming no damage to the bacterial membrane. However, the bacterial membrane in the S-ZIF-8/GO group was severely wrinkled or even broken after 808 nm light irradiation (marked with red arrows), which we attributed to the hyperthermia treatment and the ROS destruction effect of the S-ZIF-8/GO under 808 nm light irradiation. The results indicated that S-ZIF-8/GO could kill bacteria by damaging the bacterial membrane under 808 nm NIR light irradiation within 20 min. To evaluate the antibacterial mechanism of the synthesized materials, we employed an ONPG hydrolysis assay to assess the bacterial permeability of the membrane (Fig. 7d). The experimental data exhibited the highest ONPG values for the S-ZIF-8/GO group against S. aureus, showing that the bacterial permeability of the membrane of the S-ZIF-8/GO group was enhanced under synergistic photocatalytic and photothermal effects.

After the antibacterial experiment, we investigated ROS within the bacteria using DCFH-DA. According to the ROS Assay Kit, DCFH-DA was nonfluorescent and readily passed through the bacterial cell membrane into the bacteria, where esterase hydrolyzed it to create DCFH. However, the DCFH could not pass through the bacterial cell membrane, allowing the probe to be loaded easily into the bacteria. ROS in the bacteria could then oxidize DCFH to generate green fluorescence. The level of ROS produced by the bacteria was reflected in the bacterial DCF fluorescence [79]. The fluorescence images of the treated bacteria revealed that the fluorescence intensity of each group in the dark did not differ greatly from that of the Ctrl group, indicating that the material in the groups did not cause oxidative stress within the bacteria in the dark. After 20 min of 808 nm light irradiation, the S-ZIF-8/GO group exhibited the greenest fluorescence (Fig. 7e), indicating the most significant intracellular ROS production in the S-ZIF-8/GO group. This could be attributed to ROS entering the bacteria following bacterial membrane rupture during irradiation.

We studied the BCA protein leakage of bacteria. When the membrane of the bacteria was disrupted, the proteins inside the bacteria leaked out. After 808 nm light irradiation, the protein leakage of *S. aureus* cocultured with the material gradually increased with the enhanced photothermal and photocatalytic effects of the material, among which the protein leakage within the bacteria of S-ZIF-8/GO group was the largest (Fig. 7f).

There was almost no difference in the release of  $Zn^{2+}$  from S-ZIF-8/GO before and after irradiation (Fig. S9), indicating that S-ZIF-8/GO did not increase the release of  $Zn^{2+}$  during the photocatalytic sterilization process.

In conclusion, under 808 nm light irradiation, S-ZIF-8/GO generated hyperthermic,  ${}^1O_2$  and  ${}^1O_2$ . The bacterial cell membrane was destroyed, exhibiting increased permeability due to hyperthermia caused by the photothermal effect of S-ZIF-8/GO. The  ${}^1O_2$  and  ${}^1O_2$  entered more easily into the bacteria after efficiently enhancing the membrane permeation of bacteria.  ${}^1O_2$  could induce additional oxidative lesions in the cell wall and membrane, which enhanced the susceptibility of the bacteria to heat [80].  ${}^1O_2$  can degrade multiple pivotal biological molecules, such as DNA strands and membrane proteins, and influence thymidine incorporation activity in DNA synthesis, among other effects [81]. The entrance of  ${}^1O_2$  and  ${}^1O_2$  into the bacteria damaged the internal substances to destroy the bacteria (Fig. 8).

## 3.6. In vitro cytocompatibility

We assessed the cytotoxicity of the synthesized materials after 1, 3, and 7 days using an MTT assay, as displayed in Fig. S10a. ZIF-8 and ZIF-8/GO exhibited significant toxic effects on cells, perhaps due to the excessive amount of Zn ions released. The S-ZIF-8 and S-ZIF-8/GO groups exhibited excellent biocompatibility, which we attributed to the decreased release of Zn ions.

The fluorescence staining images of the cells (Fig. S10b) showed that the cells in the Ctrl group had normal morphology with complete nuclei and cytoplasm. Compared with the Ctrl group, the cell morphology of the S-ZIF-8 and S-ZIF-8/GO groups was normal, indicating that the S-ZIF-8 and S-ZIF-8/GO were not obviously cytotoxic. However, the cells in the ZIF-8 and ZIF-8/GO groups displayed a shrunken shape caused by a large release of Zn ions.

To further evaluate the safety of the samples, we performed an *in vitro* hemolysis test (Fig. S11). We used saline and DI as negative and positive controls because red blood cells could be lysed in DI at hypertonicity, whereas saline could not. After being cocultured with red blood cells for 4 h, the hemolysis rate of S-ZIF-8/GO was lower than the international standard (5 %) in all cases, demonstrating that the sample had no significant hemolytic activity.

Fig. S12 shows the release of Zn ions from ZIF-8/GO and S-ZIF-8/GO. The introduction of S significantly reduced the release of Zn ions,

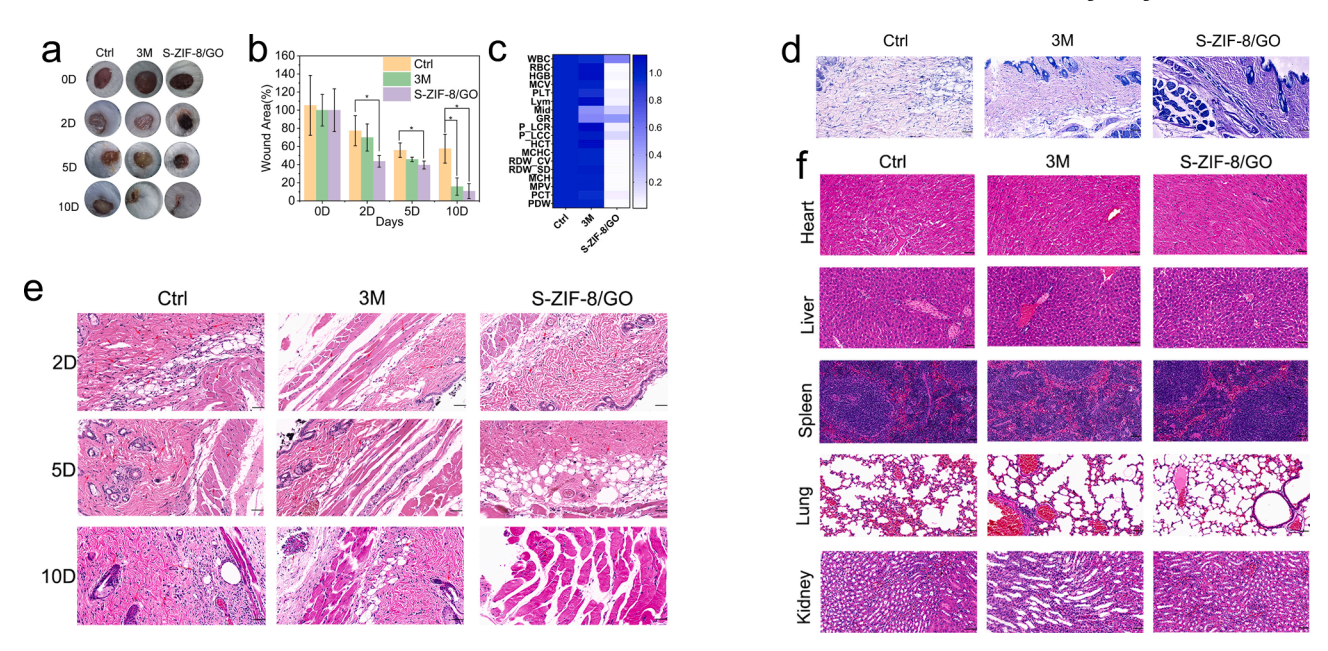


Fig. 9. a) The actual photographs of wounds at 0, 2, 5, and 10 days. b) Wound area changes statistics of Ctrl, 3 M, and S-ZIF-8/GO group with different days. c) Blood routine parameters tested after 10 days of Ctrl, 3 M, and S-ZIF-8/GO groups treatment. d) Giemsa stained images (scale bar = 50  $\mu$ m). e) H&E stained images (scale bar = 50  $\mu$ m). f) H&E staining images of the heart, liver, spleen, lung, and kidney of mice after 10 days (scale bar = 50  $\mu$ m). (n = 3, means  $\pm$  SD). \*p < 0.05, \*\*p < 0.01, \*\*\*p < 0.001.

resulting in a consequent significant reduction in the toxicity of the materials.

#### 3.7. In vivo antibacterial activity and biosafety

We assessed wound healing using mice with skin wounds, and Fig. 9a shows the wound-healing process after various periods. After undergoing treatment for 10 days, the wounds of the mice in the S-ZIF-8/GO group had largely healed, while those of the mice in the Ctrl and 3 M groups had not. We created a histogram based on the wound areas, as shown in Fig. 9b, and the wound area changes revealed that the S-ZIF-8/GO group had smaller wounds than all the other groups.

Neutrophils migrate rapidly through the circulatory system to the area of infection when a bacterial infection occurs in the body. After 10 days of treatment, we collected whole blood for routine blood analysis from all groups of mice (Fig. 9c). The results revealed that the colors of the white blood cell count (WBC), lymphocyte percentage (Lym), and neutrophil percentage (GR) in the S-ZIF-8/GO group were lighter than those of the Ctrl and 3 M groups, which revealed that the S-ZIF-8/GO group had the lowest number of inflammatory cells and the least inflammation in all the mice.

After 5 days of treatment, Giemsa staining revealed severe bacterial infections in all groups (Fig. 9d). The amounts of bacteria around the wounds in the S-ZIF-8/GO treatment group were obviously lower than those in the Ctrl and 3 M groups. Neutrophils respond to infection by rapidly migrating from the circulating blood to the site of infection, indicating the presence of a bacterial infection in the soft tissues. The H&E staining results for the wound tissue (Fig. 9e) showed many neutrophils in the Ctrl and 3 M groups (marked by red arrows). This phenomenon indicated severe bacterial infections in the wounds of the Ctrl and 3 M groups. The number of neutrophils in the S-ZIF-8/GO group was far less than that in the Ctrl and 3 M groups, and most of the cells were normal, reflecting the fact that S-ZIF-8/GO had excellent antibacterial properties and a relatively small risk of infection in the body.

Staining analysis of the mouse spleens, kidneys, livers, lungs, and hearts (Fig. 9f) showed no abnormalities in these major organs after 10 days of treatment, indicating that S-ZIF-8/GO was not significantly toxic *in vivo*.

#### 4. Conclusion

In this work, we successfully prepared S-ZIF-8/GO heterojunctions, which have excellent antibacterial effects under 808 nm light excitation. The novelty of this study is that we could adjust the band gap of ZIF-8 by doping and establishing a heterogeneous interface to achieve an excellent photoresponse under 808 nm light stimulation. Experimental and theoretical calculations confirmed that the Zn-S bond was formed by replacing S with partial N atoms in the ZIF-8 framework; the Zn-S bond provided electron transfer channels, and the combination of ZIF-8 and GO formed a built-in electric field that effectively separated electron-hole pairs. When near-infrared light irradiated S-ZIF-8/GO, the photogenerated electrons rapidly transferred from S-ZIF-8 to GO under the effect of the Zn-S bond and built-in electric field, meaning that more electrons participated in the formation of ROS, which improved the photocatalytic effect and antibacterial property of S-ZIF-8/GO. The synthesized S-ZIF-8/GO has the following advantages: stable photothermal properties, photocatalytic properties, recyclability, and an efficient 99.9 % antibacterial effect after 20 min of 808 nm light without cytotoxicity. In vivo experiments showed that S-ZIF-8/GO could accelerate wound healing and was safe in vivo. The disadvantage of S-ZIF-8/ GO was that NIR light has limited penetration, so it is restricted in treating deep tissue infections. This study offers new insights into the development of MOF-based photoexcited bactericidal materials.

#### **Declaration of Competing Interest**

The authors declare that they have no known competing financial interests or personal relationships that could have appeared to influence the work reported in this paper.

# Data availability

Data will be made available on request.

## Acknowledgments

This work is jointly supported by the National Natural Science

Foundation of China (Nos. 52173251, 51871162, 51973021), the China National Funds for Distinguished Young Scholars (No. 51925104), Beijing Municipal Health Commission (BMHC-2021-6, BMHC-2019-9, BMHC-2018-4, and PXM2020\_026275\_000002), and NSFC-Guangdong Province Joint Program (Key program no. U21A2084), and the Central Guidance on Local Science and Technology Development Fund of Hebei Province (226Z1303G).

#### Appendix A. Supplementary data

Supplementary data to this article can be found online at https://doi.org/10.1016/j.cej.2022.140857.

#### References

- B. Li, Y. Luo, Y. Zheng, X. Liu, L. Tan, S. Wu, Two-dimensional antibacterial materials, Prog. Mater. Sci. 130 (2022), 100976, https://doi.org/10.1016/j. pmatsci 2022 100976
- [2] X. Yan, J. Yang, J. Wu, H. Su, G. Sun, Y. Ni, W. Sun, Antibacterial carbon dots/iron oxychloride nanoplatform for chemodynamic and photothermal therapy, Colloid Interface Sci. Commun. 45 (2021), 100552, https://doi.org/10.1016/j.colcom/2021.100552
- [3] Y. Lin, H. Zhang, Y. Zou, K. Lu, L. Li, Y. Wu, J. Cheng, Y. Zhang, H. Chen, Q. Yu, Superhydrophobic photothermal coatings based on candle soot for prevention of biofilm formation, J. Mater. Sci. Technol. 132 (2023) 18–26, https://doi.org/ 10.1016/j.jmst.2022.06.005.
- [4] Q. Zheng, X. Liu, Y. Zheng, K.W.K. Yeung, Z. Cui, Y. Liang, Z. Li, S. Zhu, X. Wang, S. Wu, The recent progress on metal-organic frameworks for phototherapy, Chem. Soc. 50 (8) (2021) 5086–5125, https://doi.org/10.1039/D1CS00056J.
- [5] R. Gonzales, Overuse of antibiotics for acute respiratory illnesses and the epidemic of penicillin-resistant Streptococcus pneumoniae, Drug Resist. Updates 1 (4) (1998) 221–222, https://doi.org/10.1016/S1368-7646(98)80001-0.
- [6] P.S. Stewart, J. William Costerton, Antibiotic resistance of bacteria in biofilms, Lancet 358 (9276) (2001) 135–138, https://doi.org/10.1016/S0140-6736(01) 05321-1
- [7] D. Asefi, M. Arami, A.A. Sarabi, N.M. Mahmoodi, The chain length influence of cationic surfactant and role of nonionic co-surfactants on controlling the corrosion rate of steel in acidic media, Corros. Sci. 51 (8) (2009) 1817–1821, https://doi.org/ 10.1016/j.corsci.2009.05.007.
- [8] X. Wang, K. Su, L. Tan, X. Liu, Z. Cui, D. Jing, X. Yang, Y. Liang, Z. Li, S. Zhu, K.W. K. Yeung, D. Zheng, S. Wu, Rapid and highly effective noninvasive disinfection by hybrid Ag/CS@MnO<sub>2</sub> nanosheets using near-infrared light, ACS Appl. Mater. Interfaces 11 (16) (2019) 15014–15027, https://doi.org/10.1021/acsanj.8b.22136
- [9] H. Xu, W.-P. Huang, K.-F. Ren, Y.-M. Tang, Spraying layer-by-layer assembly of tannin-Fe<sup>3+</sup> and polyethyleneimine for antibacterial coating, Colloid Interface Sci. Commun. 42 (2021), 100422, https://doi.org/10.1016/j.colcom.2021.100422.
- [10] M.L. Kääriäinen, C.K. Weiss, S. Ritz, S. Pütz, D.C. Cameron, V. Mailänder, K. Landfester, Zinc release from atomic layer deposited zinc oxide thin films and its antibacterial effect on *Escherichia coli*, Appl. Surf. Sci. 287 (2013) 375–380, https://doi.org/10.1016/j.apsusc.2013.09.162.
- [11] N.M. Mahmoodi, M. Bashiri, S.J. Moeen, Synthesis of nickel–zinc ferrite magnetic nanoparticle and dye degradation using photocatalytic ozonation, Mater. Res. Bull. 47 (12) (2012) 4403–4408, https://doi.org/10.1016/j.materresbull.2012.09.036.
- [12] D. Han, Y. Han, J. Li, X. Liu, K.W.K. Yeung, Y. Zheng, Z. Cui, X. Yang, Y. Liang, Z. Li, S. Zhu, X. Yuan, X. Feng, C. Yang, S. Wu, Enhanced photocatalytic activity and photothermal effects of Cu-doped metal-organic frameworks for rapid treatment of bacteria-infected wounds, Appl. Catal. B Environ. 261 (2020), 118248, https://doi.org/10.1016/j.apcatb.2019.118248.
- [13] C. Liu, Y. Guo, X. Wei, C. Wang, M. Qu, D.W. Schubert, C. Zhang, An outstanding antichlorine and antibacterial membrane with quaternary ammonium salts of alkenes via in situ polymerization for textile wastewater treatment, Chem. Eng. J. 384 (2020), 123306, https://doi.org/10.1016/j.cej.2019.123306.
- [14] A. Almasian, M.E. Olya, N.M. Mahmoodi, Preparation and adsorption behavior of diethylenetriamine/polyacrylonitrile composite nanofibers for a direct dye removal, Fibers Polym. 16 (9) (2015) 1925–1934, https://doi.org/10.1007/ s12221-015-4624-3.
- [15] Y. Engelberg, M. Landau, The Human LL-37(17–29) antimicrobial peptide reveals a functional supramolecular structure, Nat. Commun. 11 (1) (2020) 3894, https:// doi.org/10.1038/s41467-020-17736-x.
- [16] L. Li, G. Li, Y. Wu, Y. Lin, Y. Qu, Y. Wu, K. Lu, Y. Zou, H. Chen, Q. Yu, Y. Zhang, Dual-functional bacterial cellulose modified with phase-transitioned proteins and gold nanorods combining antifouling and photothermal bactericidal properties, J. Mater. Sci. Technol. 110 (2022) 14–23, https://doi.org/10.1016/j. imst.2021.10.011.
- [17] S. Rahimi, L. Mivehi, F. Mazaheri, N.M. Mahmoodi, Degumming of Persian silk with mixed proteolytic enzymes, J. Appl. Polym. Sci. 106 (2007) 267–275, https://doi.org/10.1002/app.26492.
- [18] C.-M. Xie, X. Lu, K.-F. Wang, F.-Z. Meng, O. Jiang, H.-P. Zhang, W. Zhi, L.-M. Fang, Silver nanoparticles and growth factors incorporated hydroxyapatite coatings on metallic implant surfaces for enhancement of osteoinductivity and antibacterial

- properties, ACS Appl. Mater. Interfaces 6 (11) (2014) 8580–8589, https://doi.org/10.1021/am501428e.
- [19] A. Panáček, L. Kvítek, M. Smékalová, R. Večeřová, M. Kolář, M. Röderová, F. Dyčka, M. Šebela, R. Prucek, O. Tomanec, R. Zbořil, Bacterial resistance to silver nanoparticles and how to overcome it, Nat. Nanotechnol. 13 (1) (2018) 65–71, https://doi.org/10.1038/s41565-017-0013-y.
- [20] B. Li, L. Tan, X. Liu, Z. Li, Z. Cui, Y. Liang, S. Zhu, X. Yang, K.W. Kwok Yeung, S. Wu, Superimposed surface plasma resonance effect enhanced the near-infrared photocatalytic activity of Au@Bi<sub>2</sub>WO<sub>6</sub> coating for rapid bacterial killing, J. Hazard. Mater. 380 (2019), 120818, https://doi.org/10.1016/j.jhazmat.2019.120818.
- [21] J. Li, Z. Li, X. Liu, C. Li, Y. Zheng, K.W.K. Yeung, Z. Cui, Y. Liang, S. Zhu, W. Hu, Y. Qi, T. Zhang, X. Wang, S. Wu, Interfacial engineering of Bi<sub>2</sub>S<sub>3</sub>/Ti<sub>3</sub>C<sub>2</sub>T<sub>x</sub> MXene based on work function for rapid photo-excited bacteria-killing, Nat. Commun. 12 (1) (2021) 1224, https://doi.org/10.1038/s41467-021-21435-6.
- [22] S. Wang, L. Shang, L. Li, Y. Yu, C. Chi, K. Wang, J. Zhang, R. Shi, H. Shen, G.I.N. Waterhouse, S. Liu, J. Tian, T. Zhang, H. Liu, Phototherapy: metal-organic-framework-derived mesoporous carbon nanospheres containing porphyrin-like metal centers for conformal phototherapy, Adv. Mater. 28 (38) (2016) 8318-8318. 10.1002/adma.201670266.
- [23] Y. Cheng, Y. Chang, Y. Feng, N. Liu, X. Sun, Y. Feng, X. Li, H. Zhang, Simulated sunlight-mediated photodynamic therapy for melanoma skin cancer by titaniumdioxide-nanoparticle-gold-nanocluster-graphene heterogeneous nanocomposites, Small 13 (20) (2017) 1603935, https://doi.org/10.1002/smll.201603935.
- [24] X. Tian, Y. Sun, S. Fan, M.D. Boudreau, C. Chen, C. Ge, J.-J. Yin, Photogenerated charge carriers in molybdenum disulfide quantum dots with enhanced antibacterial activity, ACS Appl. Mater. Interfaces 11 (5) (2019) 4858–4866, https://doi.org/10.1021/acsami.8b19958.
- [25] E. Shang, J. Niu, Y. Li, Y. Zhou, J.C. Crittenden, Comparative toxicity of Cd, Mo, and W sulphide nanomaterials toward *E. coli* under UV irradiation, Environ. Pollut. 224 (2017) 606–614, https://doi.org/10.1016/j.envpol.2017.02.044.
- [26] W. Wang, Z. Zeng, G. Zeng, C. Zhang, R. Xiao, C. Zhou, W. Xiong, Y. Yang, L. Lei, Y. Liu, D. Huang, M. Cheng, Y. Yang, Y. Fu, H. Luo, Y. Zhou, Sulfur doped carbon quantum dots loaded hollow tubular g-C<sub>3</sub>N<sub>4</sub> as novel photocatalyst for destruction of *Escherichia coli* and tetracycline degradation under visible light, Chem. Eng. J. 378 (2019), 122132, https://doi.org/10.1016/j.cej.2019.122132.
- [27] B. Hayati, N.M. Mahmoodi, A. Maleki, Dendrimer-titania nanocomposite: synthesis and dye-removal capacity, Res. Chem. Intermed. 41 (6) (2015) 3743–3757, https://doi.org/10.1007/s11164-013-1486-4.
- [28] Y. Li, Z. Gao, Y. Zhang, F. Chen, P. An, H. Wu, C. You, B. Sun, MOF-shielded and glucose-responsive ultrasmall silver nano-factory for highly-efficient anticancer and antibacterial therapy, Chem. Eng. J. 416 (2021), 127610, https://doi.org/ 10.1016/j.cej.2020.127610.
- [29] N.M. Mahmoodi, M. Oveisi, M. Bakhtiari, B. Hayati, A.A. Shekarchi, A. Bagheri, S. Rahimi, Environmentally friendly ultrasound-assisted synthesis of magnetic zeolitic imidazolate framework-Graphene oxide nanocomposites and pollutant removal from water, J. Mol. Liq. 282 (2019) 115–130, https://doi.org/10.1016/j. molliq.2019.02.139.
- [30] H. Furukawa, K.E. Cordova, M. O'Keeffe, O.M. Yaghi, The chemistry and applications of metal-organic frameworks, Science 341 (6149) (2013) 1230444, https://doi.org/10.1126/science.1230444.
- [31] D.-L. Han, P.-L. Yu, X.-M. Liu, Y.-D. Xu, S.-L. Wu, Polydopamine modified CuS@ HKUST for rapid sterilization through enhanced photothermal property and photocatalytic ability, Rare Met. 41 (2) (2022) 663–672, https://doi.org/10.1007/ s12598-021-01786-1.
- [32] H.D. Lawson, S.P. Walton, C. Chan, Metal-organic frameworks for drug delivery: a design perspective, ACS Appl. Mater. Interfaces 13 (6) (2021) 7004–7020, https://doi.org/10.1021/acsami.1c01089.
- [33] Y. Luo, J. Li, X. Liu, L. Tan, Z. Cui, X. Feng, X. Yang, Y. Liang, Z. Li, S. Zhu, Y. Zheng, K.W.K. Yeung, C. Yang, X. Wang, S. Wu, Dual metal-organic framework heterointerface, ACS Cent. Sci. 5 (9) (2019) 1591–1601, https://doi.org/10.1021/ acscentsci.9b00639.
- [34] D. Han, X. Liu, S. Wu, Metal organic framework-based antibacterial agents and their underlying mechanisms, Chem. Soc. Rev. 51 (16) (2022) 7138–7169, https://doi.org/10.1039/D2CS00460G.
- [35] B. Hayati, N.M. Mahmoodi, F. Mazaheri, Dye removal from colored textile wastewater by poly(propylene imine) dendrimer: operational parameters and isotherm studies, clean: soil, air, Water 39 (2011) 673–679, https://doi.org/ 10.1002/clen.201000182.
- [36] Y. Xiao, M. Xu, N. Lv, C. Cheng, P. Huang, J. Li, Y. Hu, M. Sun, Dual stimuliresponsive metal-organic framework-based nanosystem for synergistic photothermal/pharmacological antibacterial therapy, Acta Biomater. 122 (2021) 291–305, https://doi.org/10.1016/j.actbio.2020.12.045.
- [37] X. Meng, K. Jia, K. Sun, L. Zhang, Z. Wang, Smart responsive nanoplatform via in situ forming disulfiram-copper ion chelation complex for cancer combination chemotherapy, Chem. Eng. J. 415 (2021), 128947, https://doi.org/10.1016/j. cei 2021 128947
- [38] Z. Deng, M. Li, Y. Hu, Y. He, B. Tao, Z. Yuan, R. Wang, M. Chen, Z. Luo, K. Cai, Injectable biomimetic hydrogels encapsulating Gold/metal-organic frameworks nanocomposites for enhanced antibacterial and wound healing activity under visible light actuation, Chem. Eng. J. 420 (2021), 129668, https://doi.org/ 10.1016/j.cej.2021.129668.
- [39] X. Huo, P. Zhou, J. Zhang, Y. Liu, X. Cheng, Y. Liu, W. Li, Y. Zhang, N, S-Doped porous carbons for persulfate activation to remove tetracycline: Nonradical mechanism, J. Hazard. Mater. 391 (2020), 122055, https://doi.org/10.1016/j.jhazmat.2020.122055.

- [40] W. Tian, H. Zhang, X. Duan, H. Sun, M.O. Tade, H.M. Ang, S. Wang, Nitrogen- and sulfur-codoped hierarchically porous carbon for adsorptive and oxidative removal of pharmaceutical contaminants, ACS Appl. Mater. Interfaces 8 (11) (2016) 7184–7193, https://doi.org/10.1021/acsami.6b01748.
- [41] B. Zhu, H. Tan, J. Fan, B. Cheng, J. Yu, W. Ho, Tuning the strength of built-in electric field in 2D/2D g-C<sub>3</sub>N<sub>4</sub>/SnS<sub>2</sub> and g-C<sub>3</sub>N<sub>4</sub>/ZrS<sub>2</sub> S-scheme heterojunctions by nonmetal doping, J. Materiom. 7 (5) (2021) 988–997, https://doi.org/10.1016/j. imat.2021.02.015.
- [42] K. Su, L. Tan, X. Liu, Z. Cui, Y. Zheng, B. Li, Y. Han, Z. Li, S. Zhu, Y. Liang, X. Feng, X. Wang, S. Wu, Rapid photo-sonotherapy for clinical treatment of bacterial infected bone implants by creating oxygen deficiency using sulfur doping, ACS Nano 14 (2) (2020) 2077–2089, https://doi.org/10.1021/acsnano.9b08686.
- [43] H. Chen, X. Yuan, L. Jiang, H. Wang, H. Yu, X. Wang, Intramolecular modulation of iron-based metal organic framework with energy level adjusting for efficient photocatalytic activity, Appl. Catal. B Environ. 302 (2022), 120823, https://doi. org/10.1016/j.apcatb.2021.120823.
- [44] T. Cai, L. Wang, Y. Liu, S. Zhang, W. Dong, H. Chen, X. Yi, J. Yuan, X. Xia, C. Liu, S. Luo, Ag<sub>3</sub>PO<sub>4</sub>/Ti<sub>3</sub>C<sub>2</sub> MXene interface materials as a Schottky catalyst with enhanced photocatalytic activities and anti-photocorrosion performance, Appl. Catal. B Environ. 239 (2018) 545–554, https://doi.org/10.1016/j. apcatb.2018.08.053.
- [45] X. Xie, C. Mao, X. Liu, L. Tan, Z. Cui, X. Yang, S. Zhu, Z. Li, X. Yuan, Y. Zheng, K.W. K. Yeung, P.K. Chu, S. Wu, Tuning the bandgap of photo-sensitive polydopamine/Ag<sub>3</sub>PO<sub>4</sub>/graphene oxide coating for rapid, noninvasive disinfection of implants, ACS Cent. Sci. 4 (6) (2018) 724–738, https://doi.org/10.1021/acscentsri\_8b00177
- [46] D. Asefi, N.M. Mahmoodi, M. Arami, Effect of nonionic co-surfactants on corrosion inhibition effect of cationic gemini surfactant, Colloids Surf. A 355(1) (2010) 183-186. 10.1016/j.colsurfa.2009.12.019.
- [47] W. Wang, B. Xu, X. Pan, J. Zhang, H. Liu, Solvent-dependent adsorption-driven mechanism for MOFs-based yolk-shell nanostructures, Angew. Chem. Int. Ed. 60 (14) (2021) 7802-7808. 10.1002/anie.202014895.
- [48] Y. Lin, D. Han, Y. Li, L. Tan, X. Liu, Z. Cui, X. Yang, Z. Li, Y. Liang, S. Zhu, S. Wu, Ag<sub>2</sub>S@WS<sub>2</sub> heterostructure for rapid bacteria-killing using near-infrared light, ACS Sustain. Chem. Eng. 7 (17) (2019) 14982–14990, https://doi.org/10.1021/acssuschemeng.9b03287.
- [49] Z. Liu, L. Tan, X. Liu, Y. Liang, Y. Zheng, K.W.K. Yeung, Z. Cui, S. Zhu, Z. Li, S. Wu, Zn<sup>2+</sup>-assisted photothermal therapy for rapid bacteria-killing using biodegradable humic acid encapsulated MOFs, Colloids Surf. B 188 (2020), 110781, https://doi.org/10.1016/j.colsurfb.2020.110781.
- [50] Q. Xia, B. Huang, X. Yuan, H. Wang, Z. Wu, L. Jiang, T. Xiong, J. Zhang, G. Zeng, H. Wang, Modified stannous sulfide nanoparticles with metal-organic framework: Toward efficient and enhanced photocatalytic reduction of chromium (VI) under visible light, J. Colloid Interface Sci. 530 (2018) 481–492, https://doi.org/10.1016/j.jcis.2018.05.015.
- [51] T. Zhu, S. Xu, F. Yu, X. Yu, Y. Wang, ZIF-8@GO composites incorporated polydimethylsiloxane membrane with prominent separation performance for ethanol recovery, J. Membr. Sci. 598 (2020), 117681, https://doi.org/10.1016/j. memsci.2019.117681.
- [52] F.J. Martín-Jimeno, F. Suárez-García, J.I. Paredes, M. Enterría, M.F.R. Pereira, J. I. Martins, J.L. Figueiredo, A. Martínez-Alonso, J.M.D. Tascón, A "nanopore lithography" strategy for synthesizing hierarchically micro/mesoporous carbons from ZIF-8/graphene oxide hybrids for electrochemical energy storage, ACS Appl. Mater. Interfaces 9 (51) (2017) 44740–44755, https://doi.org/10.1021/acsami.7b16567.
- [53] J. Wang, Y. Wang, Y. Zhang, A. Uliana, J. Zhu, J. Liu, B. Van der Bruggen, Zeolitic imidazolate framework/graphene oxide hybrid nanosheets functionalized thin film nanocomposite membrane for enhanced antimicrobial performance, ACS Appl. Mater. Interfaces 8 (38) (2016) 25508–25519, https://doi.org/10.1021/ acsami.6b06992.
- [54] M. Wang, L. Nian, Y. Cheng, B. Yuan, S. Cheng, C. Cao, Encapsulation of colloidal semiconductor quantum dots into metal-organic frameworks for enhanced antibacterial activity through interfacial electron transfer, Chem. Eng. J. 426 (2021), 130832, https://doi.org/10.1016/j.cej.2021.130832.
- [55] Y. Li, X. Liu, L. Tan, Z. Cui, X. Yang, Y. Zheng, K.W.K. Yeung, P.K. Chu, S. Wu, Rapid sterilization and accelerated wound healing using Zn<sup>2+</sup> and graphene oxide modified g-C<sub>3</sub>N<sub>4</sub> under dual light irradiation, Adv. Funct. Mater. 28 (30) (2018) 1800299, https://doi.org/10.1002/adfm.201800299.
- [56] S.R. Mousavi, M. Asghari, N.M. Mahmoodi, Chitosan-wrapped multiwalled carbon nanotube as filler within PEBA thin film nanocomposite (TFN) membrane to improve dye removal, Carbohydr. Polym. 237 (2020), 116128, https://doi.org/ 10.1016/j.carbool.2020.116128.
- [57] F. Hosseini, S. Sadighian, H. Hosseini-Monfared, N.M. Mahmoodi, Dye removal and kinetics of adsorption by magnetic chitosan nanoparticles, Desalin. Water Treat. 57 (51) (2016) 24378–24386, https://doi.org/10.1080/19443994.2016.1143879.
- [58] A. Almasian, N.M. Mahmoodi, M.E. Olya, Tectomer grafted nanofiber: Synthesis, characterization and dye removal ability from multicomponent system, J. Ind. Eng. Chem. 32 (2015) 85–98, https://doi.org/10.1016/j.jiec.2015.08.002.
- [59] N.M. Mahmoodi, M. Ghezelbash, M. Shabanian, F. Aryanasab, M.R. Saeb, Efficient removal of cationic dyes from colored wastewaters by dithiocarbamatefunctionalized graphene oxide nanosheets: From synthesis to detailed kinetics studies, J. Taiwan Inst. Chem. Eng. 81 (2017) 239–246, https://doi.org/10.1016/j. jtice.2017.10.011.
- [60] H. Wang, Y. Bian, J. Hu, L. Dai, Highly crystalline sulfur-doped carbon nitride as photocatalyst for efficient visible-light hydrogen generation, Appl. Catal. B 238 (2018) 592–598, https://doi.org/10.1016/j.apcatb.2018.07.023.

- [61] Q. Liang, M. Zhang, C. Liu, S. Xu, Z. Li, Sulfur-doped graphitic carbon nitride decorated with zinc phthalocyanines towards highly stable and efficient photocatalysis, Appl. Catal. A 519 (2016) 107–115, https://doi.org/10.1016/j. aprata 2016 03 033
- [62] B. Cao, H. Liu, X. Zhang, P. Zhang, Q. Zhu, H. Du, L. Wang, R. Zhang, B. Xu, MOF-derived ZnS nanodots/Ti<sub>3</sub>C<sub>2</sub>Tx MXene hybrids boosting superior lithium storage performance, Nano-Micro Lett. 13 (1) (2021) 202, https://doi.org/10.1007/sept.2010.0728.x
- [63] X. Wang, Z. Cao, B. Du, Y. Zhang, R. Zhang, Visible-light-driven zeolite imidazolate frameworks-8@ZnO composite for heavy metal treatment, Compos. Part B 183 (2020), 107685, https://doi.org/10.1016/j.compositesb.2019.107685.
- [64] F. Yang, J. Xie, X. Liu, G. Wang, X. Lu, Linker defects triggering boosted oxygen reduction activity of Co/Zn-ZIF nanosheet arrays for rechargeable Zn-air batteries, Small 17 (3) (2021) e2007085.
- [65] G. Chaturvedi, A. Kaur, S.K. Kansal, CdS-decorated MIL-53(Fe) microrods with enhanced visible light photocatalytic performance for the degradation of ketorolac tromethamine and mechanism insight, J. Phys. Chem. C 123 (27) (2019) 16857–16867, https://doi.org/10.1021/acs.jpcc.9b04312.
- [66] J. Zeng, D. Goldfeld, Y. Xia, A plasmon-assisted optofluidic (PAOF) system for measuring the photothermal conversion efficiencies of gold nanostructures and controlling an electrical switch, Angew. Chem. Int. Ed. Engl. 52 (15) (2013) 4169–4173, https://doi.org/10.1002/anie.201210359.
- [67] Q. Tian, F. Jiang, R. Zou, Q. Liu, Z. Chen, M. Zhu, S. Yang, J. Wang, J. Wang, J. Hu, Hydrophilic Cu<sub>9</sub>S<sub>5</sub> nanocrystals: a photothermal agent with a 25.7% heat conversion efficiency for photothermal ablation of cancer cells in vivo, ACS Nano 5 (12) (2011) 9761–9771, https://doi.org/10.1021/nn203293t.
- [68] C. Mao, W. Zhu, Y. Xiang, Y. Zhu, J. Shen, X. Liu, S. Wu, K.M.C. Cheung, K.W. K. Yeung, Enhanced near-infrared photocatalytic eradication of MRSA biofilms and osseointegration using oxide perovskite-based P-N heterojunction, Adv. Sci. 8 (15) (2021) 2002211, https://doi.org/10.1002/advs.202002211.
- [69] J. Jin, J.P. Kim, S. Wan, K.H. Kim, Y. Choi, P. Li, J. Kang, Z. Ma, J.H. Lee, O. Kwon, D.W. Kim, J.H. Park, Hierarchical pore enhanced adsorption and photocatalytic performance of graphene oxide/Ti-based metal-organic framework hybrid for toluene removal, Appl. Catal. B 317 (2022), 121751, https://doi.org/10.1016/j.apcatb.2022.121751.
- [70] M. Wang, K. Deng, W. Lu, X. Deng, K. Li, Y. Shi, B. Ding, Z. Cheng, B. Xing, G. Han, Z. Hou, J. Lin, Rational design of multifunctional Fe@gamma-Fe<sub>2</sub>O<sub>3</sub> @H-TiO<sub>2</sub> nanocomposites with enhanced magnetic and photoconversion effects for wide applications: from photocatalysis to imaging-guided photothermal cancer therapy, Adv. Mater. 30 (13) (2018) e1706747.
- [71] J. Liao, W. Cui, J. Li, J. Sheng, H. Wang, X.A. Dong, P. Chen, G. Jiang, Z. Wang, F. Dong, Nitrogen defect structure and NO+ intermediate promoted photocatalytic NO removal on H<sub>2</sub> treated g-C<sub>3</sub>N<sub>4</sub>, Chem. Eng. J. 379 (2020), 122282, https://doi.org/10.1016/j.cej.2019.122282.
- [72] S. Cao, B. Fan, Y. Feng, H. Chen, F. Jiang, X. Wang, Sulfur-doped g-C<sub>3</sub>N<sub>4</sub> nanosheets with carbon vacancies: General synthesis and improved activity for simulated solar-light photocatalytic nitrogen fixation, Chem. Eng. J. 353 (2018) 147–156, https://doi.org/10.1016/j.cej.2018.07.116.
- [73] T. Wang, L. Liu, G. Ge, M. Liu, W. Zhou, K. Chang, F. Yang, D. Wang, J. Ye, Two-dimensional titanium oxide nanosheets rich in titanium vacancies as an efficient cocatalyst for photocatalytic water oxidation, J. Catal. 367 (2018) 296–305, https://doi.org/10.1016/j.jcat.2018.09.026.
- [74] W. Chen, Y. Wu, Y. Yue, J. Liu, W. Zhang, X. Yang, H. Chen, E. Bi, I. Ashraful, M. Grätzel, L. Han, Efficient and stable large-area perovskite solar cells with inorganic charge extraction layers, Science 350 (6263) (2015) 944–948, https://doi.org/10.1126/science.aad1015.
- [75] X. Yu, J. Xie, Q. Liu, H. Dong, Y. Li, The origin of enhanced photocatalytic activity in g-C<sub>3</sub>N<sub>4</sub>/TiO<sub>2</sub> heterostructure revealed by DFT calculations, J. Colloid Interface Sci. 593 (2021) 133–141, https://doi.org/10.1016/j.jcis.2021.02.103.
- [76] J. Liu, Origin of high photocatalytic efficiency in monolayer g-C<sub>3</sub>N<sub>4</sub>/CdS heterostructure: a hybrid DFT study, J. Phys. Chem. C 119 (51) (2015) 28417–28423, https://doi.org/10.1021/acs.jpcc.5b09092.
- [77] J. Li, S. Song, J. Meng, L. Tan, X. Liu, Y. Zheng, Z. Li, K.W.K. Yeung, Z. Cui, Y. Liang, S. Zhu, X. Zhang, S. Wu, 2D MOF periodontitis photodynamic ion therapy, J. Am. Chem. Soc. 143 (37) (2021) 15427–15439, https://doi.org/10.1021/ jacs.1c07875.
- [78] X. Feng, J. Lei, L. Ma, Q. Ouyang, Y. Zeng, H. Liang, C. Lei, G. Li, L. Tan, X. Liu, C. Yang, Ultrasonic interfacial engineering of MoS<sub>2</sub>-modified Zn single-atom catalysts for efficient osteomyelitis sonodynamic ion therapy, Small 18 (8) (2022) 2105775, https://doi.org/10.1002/smll.202105775.
- [79] C. Mao, Y. Xiang, X. Liu, Y. Zheng, K.W.K. Yeung, Z. Cui, X. Yang, Z. Li, Y. Liang, S. Zhu, S. Wu, Local photothermal/photodynamic synergistic therapy by disrupting bacterial membrane to accelerate reactive oxygen species permeation and protein leakage, ACS Appl. Mater. Interfaces 11 (19) (2019) 17902–17914, https://doi.org/10.1021/acsami.9b05787.
- [80] L. Tan, J. Li, X. Liu, Z. Cui, X. Yang, S. Zhu, Z. Li, X. Yuan, Y. Zheng, K.W.K. Yeung, H. Pan, X. Wang, S. Wu, Rapid biofilm eradication on bone implants using red phosphorus and near-infrared light, Adv. Mater. 30 (31) (2018) 1801808, https:// doi.org/10.1002/adma.201801808.
- [81] Y. Li, X. Liu, L. Tan, Z. Cui, D. Jing, X. Yang, Y. Liang, Z. Li, S. Zhu, Y. Zheng, K.W. K. Yeung, D. Zheng, X. Wang, S. Wu, Eradicating multidrug-resistant bacteria rapidly using a multi functional g-C<sub>3</sub>N<sub>4</sub>@Bi<sub>2</sub>S<sub>3</sub> nanorod heterojunction with or without antibiotics, Adv. Funct. Mater. 29 (20) (2019) 201900946, https://doi.org/10.1002/adfm.201900946.